A cohesive phase-field fracture model for chemo-mechanical environments: Studies on degradation in battery materials

Shahed Rezaei[1,*], Jacob Niikoi Okoe-Amon[1], Cerun Alex Varkey[1], Armin Asheri[1,2], Hui Ruan[1], Bai-Xiang Xu[1,*]

[1] *Mechanics of Functional Materials Division, Institute of Materials Science, Technische Universität Darmstadt, Darmstadt 64287, Germany*

[2] *Volkswagen AG, Berliner Ring 2, Wolfsburg 38436, Germany*

[*] *corresponding authors: s.rezaei@mfm.tu-darmstadt.de, xu@mfm.tu-darmstadt.de*

Abstract

In the context of computational modeling of fracture in chemo-mechanical environments, physically-sound and strong coupling between different fields is essential. Furthermore, our knowledge of the fracture in a purely mechanical setting should be extended to the new realm adequately. In this work, we apply the cohesive phase-field (CPF) fracture models to address damage initiation and progression in a chemo-mechanical coupled environment. Since CPF models are shown to be independent of the length scale parameter, such models allow a unified simulation framework for bulk and interface damages that concurrently and competitively occur in the battery materials. First, a thermodynamical framework is discussed to obtain all the possible coupling terms consistently. Through a systematic derivation from dissipation inequality and by performing various studies, we intend to comparatively demonstrate the role of different coupling terms and their impact on the obtained results. Specifically, we focus on (1) the influence of the stress field as well as the damage variable on the flux vector, (2) concentration-dependent fracture properties, (3) advantages of cohesive phase-field formulation in the multiphysics environment, and (4) influence of phase-transformation on the cracking mechanism in solids. Finally, we present some initial studies on a simplified system of a solid-state battery system, where cracking inside a single crystalline active material surrounded by a solid electrolyte is under focus. The results of the study show the dominant crack patterns. Such investigations open up opportunities for better design of battery microstructures and enhance their lifetime and performance at the cell level.

Keywords: chemo-mechanical fracture, cohesive phase-field damage, solid-state batteries

1. Introduction

Owing to their high specific energy and power density, lithium-ion batteries (LIBs) showed great potential in various applications from portable electronics to large-scale grids for harvesting electrical energy from renewable sources. As a result of increasing demands for electrification, extensive research is motivated to fabricate electrodes, especially cathodes

that are safe and have high energy densities. A recent trend for improving battery performance focuses on replacing liquid electrolytes with solid electrolytes (SE) which enhances battery safety and energy density [1]. However, all-solid-state batteries (ASSBs) exhibit performance fading in the charge/discharge process of ASSBs that is normally caused by the material degradation of anodes, cathodes, and electrolytes as well as the interface between electrodes/electrolytes. See also [2] for a perspective that highlights the coupling between electrochemistry, mechanics, and geometry in positive electrodes of Li-ion batteries.

1.1. Damage mechanisms in all-solid-state batteries

One prototype ASSB consists of solid Li as an anode, solid-state material for the SE, and a composite structure for the cathode side. In Fig. 1, the micro-scale view of a battery cell is shown. The composite cathode usually consists of spherical particles known as active materials (AM) which are surrounded by the SE. Each of these particles may consist of complex morphologies of grains and grain boundaries (GB) [3]. As an example, the polycrystalline $LiNi_xMn_yCo_zO_2$ (NMC) material is a promising choice for LIBs due to its high capacity and electrochemical stability.

When Li is intercalating into the host material, electrodes deform with a characteristic volumetric strain. Fracture is a consequence of repetitive, inhomogeneous deformation and hinders ionic or electron transport which leads to resistance increase and capacity fade. Therefore, a significant challenge in all-solid-state batteries lies in integrating solid electrolytes with the other components of the battery [4, 5]. Specifically, the interfaces between the solid electrolyte and electrode materials present fundamental scientific and engineering challenges.

Crack propagation at the microscale of a battery system can be divided into damage at interfaces and damage within solid parts. We try to further break these complexities into the following main points which are also shown in Fig. 1. Note there are also different yet very similar mechanisms such as delamination between the current collectors and anode or cathode part and crack developments within the anode material that are not further explained here. On the cathode side, transgranular fracture within the active material particles may happen [6]. Cracking happens within the solid electrolyte as well [7, 8]. This includes crack progression and void growth from the anode side, as well as Li-dendrite induced (intergranular) fracture in crystalline solid electrolyte [9, 10, 11, 12, 13, 14]. Here, microcracks tend to nucleate and propagate at the edge of an electrolyte which at some point leads to electrolyte failure [15]. Intergranular fracture can happen within the active material particles. See for example studies reported in [16, 17, 18, 19, 20, 21]. Finally, for the case of solid-state batteries, one should consider delamination at the interface between the active material and the solid electrolyte [22, 23, 24, 25]. The above-mentioned arguments make it clear that proper numerical simulations are needed for a better design of crack-free solid-state battery systems that impede dendrite nucleation as well. The above review also indicated that bulk and interface damage happen concurrently and competitively. Therefore, a unified model for bulk and interface fracture simulation is desirable as it can simplify the numerical studies and therefore severely speed up the material design procedure. For this purpose, we try to argue that the cohesive phase-field model is a promising candidate.

Considering fracture in a chemo-mechanical environment, the following points have to be addressed. First, the concentration field affects the mechanical part through chemical

strain or concentration-dependent elastic properties. Furthermore, the damage field (crack initiation and progression) is also under the influence of the concentration field. As an example, in some applications, Lithium or Hydrogen embrittlement comes into the picture [3, 16, 26]. On the other hand, damage progression and mechanical stresses severally change the chemical flux and therefore the species' concentration through the process. Readers are also encouraged to see [27, 28, 1, 5, 29] for a review of the above-mentioned phenomena within battery systems. For reviews on available computational models see [30, 31]. The above points are summarized on the bottom-left side of Fig. 1, where we emphasize the necessity of a full coupling between different involved fields.

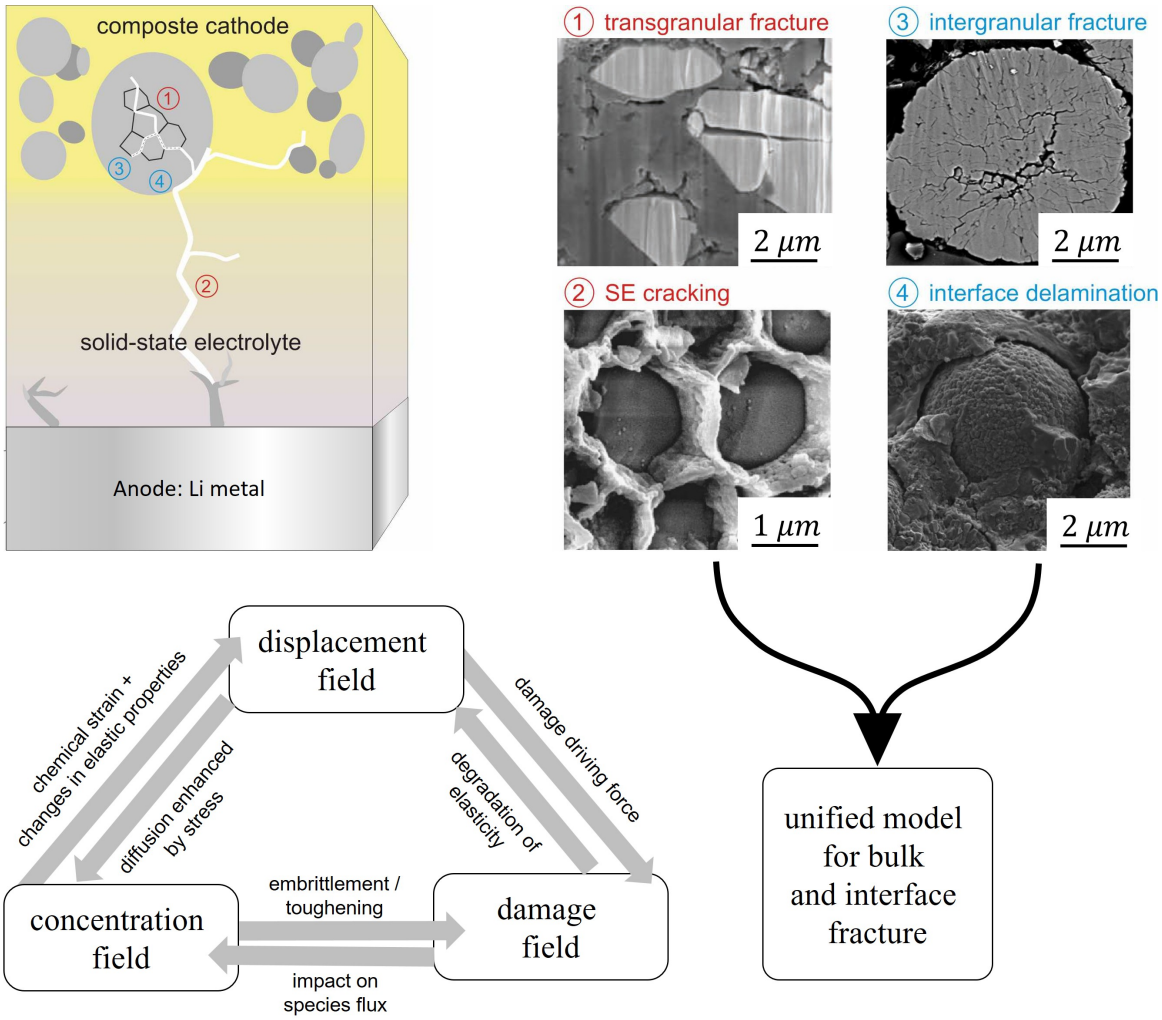

Figure 1: Top left: schematic representation of an all-solid-state battery at the particle level and its degradation mechanisms. Top right: experimental observation on different active damage mechanisms (1) cracking through the active-material grains [6], (2) solid-state electrolyte cracking and dendrite growth at cracked surfaces [7, 32], (3) grain boundary cracking within the active material [18] and (4) fracture at the interface between the active material and solid electrolyte [24]. Bottom left: summary of coupling terms between involved physics.

1.2. Advances on phase-field damage modeling

Phase-field (PF) damage formulations showed great potential in predicting crack nucleation, propagation, and branching in various applications at different scales [33, 34]. In PF brittle fracture models, the critical energy release rate is fully attributed to the surface energy, which is distributed in a diffuse damage zone. These methods rely on introducing an additional parameter usually referred to as the length scale parameter l_c [35, 36]. Furthermore, it is shown that by manipulating the gradient term in the formulation, one can model anisotropic crack propagation (see [37] and reference therein). The internal length scale parameter in AT1 and AT2 PF damage models is related to material strength and other material properties and should be treated as a material property [38, 39]. See also numerical studies in [40] and the review of phase-field damage models in [41].

It is important to note that when other physics such as chemical diffusion are taken into account, the fracture properties (including strength and fracture energy) may vary as well. The latter observation implies that the length scale parameter should also be a function of concentration which is not desirable as we would like to keep it as a numerical parameter.

Some recent developments managed to combine cohesive zone and phase-field fracture models [42, 43, 44]. The main idea is to take into account the gradual evolution of the fracture energy. Wu and Nguyen [45] proposed a new phase-field fracture model which takes into account the cohesive nature of the fracture. In this new modeling approach in addition to the fracture energy, the material ultimate strength is also a direct input for the model As a result, the new PF formulation is shown to be almost length-scale independent considering the crack path and overall system response [46, 47].s

1.3. chemo-mechanical coupled phase-field damage models

Although the main focus is on battery systems, here we review some relevant contributions in other contexts as well. The common ground between these contributions is particularly phase-field damage models in chemical environments. Numerical studies on damage inside battery systems initiated by some authors in the last few years. Miehe et al. [48] proposed a finite strain theory for chemo-elasticity coupled with PF modeling of fracture. The authors also incorporate gradient-extended Cahn-Hilliard-type diffusion for the Li-ions to account for phase segregation. Zhang et al. [49] formulated a variational-based coupled chemo-mechanical computational framework to study diffusion-induced large plastic deformation and phase-field fracture in Si electrodes. See also [50] for similar studies. Zuo and Zhao [51] established a PF model coupling lithium diffusion and stress evolution with crack propagation. The authors explored the coupling effects on diffusion and crack propagation paths within a silicon thin film electrode. Klinsmann et al. [52] applied a coupled model of mechanical stress, lithium diffusion, and PF fracture approach and studied crack growth during lithium insertion or extraction. See also [53, 54]. Xu et al. [55] presented a finite strain PF fracture model which includes phase segregation, fracture, and the related electrochemical reaction in a systematic manner. The authors managed to account for the reaction on the freshly generated diffusive fracture surface. Mesgarnejad and Karma [56] investigated the fracture of Li-ion battery cathodic particles using a PF approach and studied the role of flaw size, flux, and particle size for 2D disks and 3D spherical particles. Narayan and Anand [57] developed a numerical model for the process of plating-and-stripping of lithium which can result in the decohesion of the Li/SE interface, and fracture of the solid-electrolyte.

Liu and Xu [58] developed a multiphysics model utilizing the PF damage method for silicon nanoparticles and concluded that the lithiation rate and particle size are the dominant factors for crack initiation and propagation. Boyce et al. [59] utilized X-ray computed tomography imaging and combined an electro-chemo-mechanical model with a PF fracture model to study cracking in the electrode particles of a realistic battery microstructure.

Finally, it is worth mentioning some available damage models for battery systems which are based on the application of cohesive zone models [60, 61, 62]. These models are certainly very beneficial when it comes to interface cracking between different phases [63, 16] or solid parts [3]. Nevertheless, they are not capable of predicting arbitrary cracking within the composite cathode (see also different fracture modes listed in Fig. 1). Investigations by [64] show the promising direction in integrating the interface and bulk to address inter and intra-granular fracture in battery systems (see also [65]).

Fracture in chemo-mechanical coupled environments has applications in various other fields such as hydrogen embitterment and hydraulic fracture. Most of these applications are related to the new generation materials for energy storage and transfer. Di Leo and Anand [66] formulated a consistent theory that takes into account the diffusion of hydrogen as well as large elastic-plastic deformations within a solid. Salvadori et al. [67] proposed a model for mass and heat transport, mechanics, and chemical reactions. The authors demonstrated the application of the model in different case studies such as vacancies redistribution in metals, hydrogen embrittlement, and the charge-discharge of active particles in Li-ion batteries. Martínez-Pañeda et al. [68] studied crack growth in the presence of hydrogen using a PF damage model. Duda et al. [69] developed a PF theory of fracture in elastoplastic solids which accounts for both solute-induced deformation and solute-assisted fracture. See also [70, 71, 72]. The previously mentioned works are based on the so-called standard PF damage model in which the length-scale parameter determines the strength of the material. Utilizing cohesive PF damage models, one has direct control over the concentration-dependent fracture properties of the formulation. Recently, Wu et al. [73] applied the PF regularized cohesive zone model in the context of hydrogen-assisted cracking and showed the global responses are insensitive to both the mesh discretization resolution and the length scale parameter.

1.4. Outline of the present paper

Despite the reviewed progress, some fundamental questions remain unanswered when it comes to the multiphysics fracture. For example, the influence of the damage variable on the species' flux and vice-versa is often ignored. Furthermore, including concentration-dependent fracture properties based on thermodynamic derivation is not considered in most of the formulations. Finally, the impact of the chosen internal length scale for fracture in multiphysics environments requires much more attention. We show the necessity of taking the cohesive nature of fracture as well as consistent derivation based on dissipation inequality to include all the active coupling terms into account.

In section 2, we present a step-by-step derivation of a chemo-mechanical coupled damage model based on thermodynamic laws. In section 3, the residuals and their discretized form in a finite element code utilizing automatic differentiation for solving the equations are described. In section 4, the numerical examples are presented where we show the influence of different coupling terms and how the introduced model can be applied to study the crack patterns in all-solid-state batteries. Finally, the concluding points are discussed.

2. Formulation

2.1. Various types of coupling

According to how strong the connections between different physics are, various coupling terms are needed to properly describe the problem. With an emphasis on the chemomechanical coupled environment, we summarize coupling scenarios in Fig. 1. Here we have three main fields which are connected together in two ways. As an example, the concentration field results in additional chemical strain due to the molar expansion of the lattice. On the other hand, the stress field within the solids will enhance the chemical diffusion (e.g. we observe the concentration of species at the crack tip). More details of these terms are provided in what follows in the current section.

In the current work, we argue why some of these coupling terms appear during the consistent derivation. Next, we shall study their influence on the obtained results that severely impact the model prediction.

2.2. Kinematics

It is assumed that the bulk undergoes elastic deformation together with a brittle or quasi-brittle fracture at small deformation based on isothermal and adiabatic conditions.

Let's consider the configuration of the body V as shown in the middle part of Fig. 2. The latter represents a simplified version of a composite cathode in solid-state batteries.

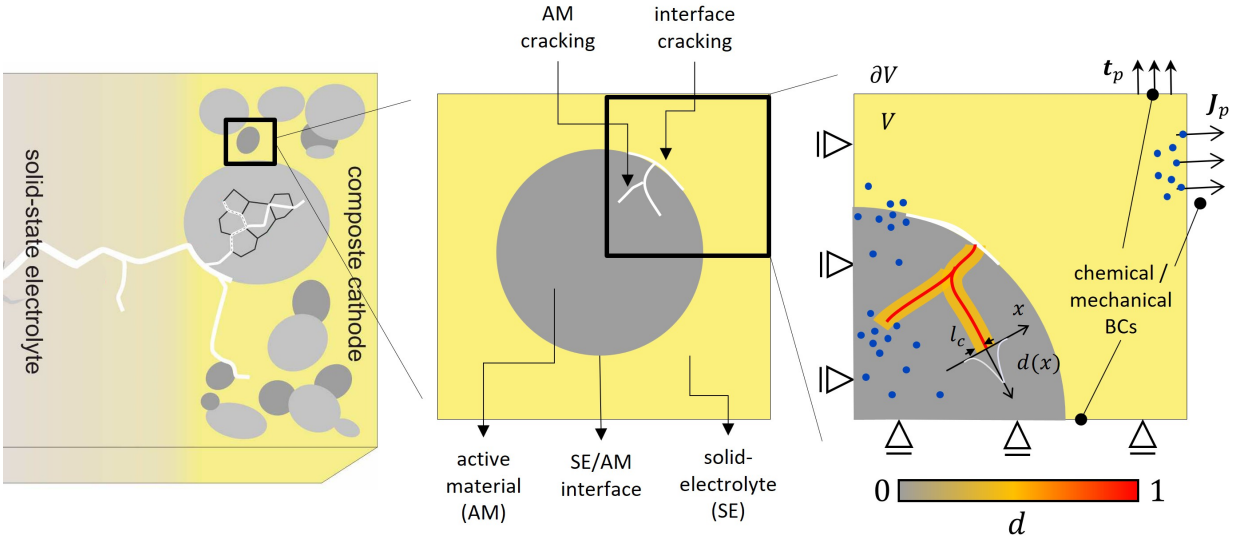

Figure 2: Microstructure of a solid-state battery system. Fracture within the active material is modeled by a smeared approach utilizing a phase-field damage model. The mechanical and chemical boundary conditions are shown on the right-hand side.

The material volume change due to the concentration field is captured by the additional chemical strain tensor $\boldsymbol{\varepsilon}_c$ which is assumed to be proportional to the concentration of species:

$$\boldsymbol{\varepsilon}_c = (c - c_0)\ \boldsymbol{\Omega}, \quad \boldsymbol{\Omega} = \Omega_{ij}\ \boldsymbol{e}_i \otimes \boldsymbol{e}_j. \tag{1}$$

Here, c is the Li concentration, and c_0 is the initial concentration within the material. In the case of isotropic chemical strain, $\Omega_{ij} = \Omega/3$ for $i = j$ and $\Omega_{ij} = 0$ for $i \neq j$. The

scalar parameter Ω is the partial molar volume. The relation in Eq. 1 gets more complicated for specific material [74]. The defined material properties throughout this work can be any arbitrary function of space (i.e. $\boldsymbol{\Omega}(\boldsymbol{x})$) due to heterogeneity within the system.

The total strain tensor $\boldsymbol{\varepsilon}$, kinematically related to the displacement field $\boldsymbol{u}$, is obtained via the symmetric part of the displacement gradient tensor. Here, it is assumed that the strain tensor can be additively decomposed to elastic $\boldsymbol{\varepsilon}_e$ and chemical part $\boldsymbol{\varepsilon}_c$, respectively.

$$\boldsymbol{\varepsilon} = \frac{1}{2}(\nabla \boldsymbol{u} + \nabla \boldsymbol{u}^T) = \boldsymbol{\varepsilon}_e + \boldsymbol{\varepsilon}_c. \tag{2}$$

A smeared approach for fracture is utilized in this work where sharp cracks are replaced by a diffuse damage zone. Such non-local methodologies solve the issue with mesh objectivity when it comes to softening due to damage. Phase-field damage models are among the non-local methods in which the energy related to the creation of free surfaces is dissipated in a diffuse damage zone by employing the crack density function γ. These methods rely on introducing an additional parameter usually referred to as the length scale parameter l_c [35, 36]. Defining the damage parameter and its spatial gradient by d and ∇d, one can write the crack (free surface) energy as:

$$\Psi_d = \int_\Gamma G_c \; d\Gamma = \int_\Omega G_c \; \gamma(d, \nabla d) \; d\Omega. \tag{3}$$

2.3. Dissipation inequality

The second law of thermodynamics in terms of the Clausius-Duhem inequality is utilized to derive thermodynamically consistent constitutive relations of the model (see Eq. 4). See Appendix A for a detailed derivation of this relation in a chemo-mechanical coupled environment. Taking into consideration an isothermal and adiabatic system, the local form of the dissipation inequality is given as:

$$\boldsymbol{\sigma} : \dot{\boldsymbol{\varepsilon}} - \dot{\psi} + (\nabla \cdot \boldsymbol{\zeta}) \, \dot{c} + \boldsymbol{\zeta} \cdot \nabla \dot{c} + \mu \dot{c} - \boldsymbol{J} \cdot \nabla \mu + Y \dot{d} + \boldsymbol{H} \cdot \nabla \dot{d} \geq 0. \tag{4}$$

In the above equation, $\boldsymbol{\sigma}$ denotes the Cauchy stress tensor, ψ is the bulk total free energy density, μ is the chemical potential, $\boldsymbol{J}$ is the chemical flux vector, Y is the damage driving force and $\boldsymbol{H}$ is the work conjugate force related to ∇d. $\nabla \cdot \boldsymbol{\zeta}$ is the scalar microscopic stress that expands power over the rate $\dot{c}$. More details on the definition of each term will be provided in what follows and for more information, the reader is referred to Appendix A. Next, we define the total free energy density of the system as a function of strain $\boldsymbol{\varepsilon}$, concentration c, concentration gradient ∇c, damage parameter d, and damage gradient ∇d. The total energy is divided into the elastic part ψ_e, chemical part ψ_c and damage part ψ_d:

$$\psi(\boldsymbol{\varepsilon}, c, \nabla c, d, \nabla d) = \psi_e(\boldsymbol{\varepsilon}, c, d) + \psi_c(c, \nabla c) + \psi_d(c, d, \nabla d). \tag{5}$$

Details on the choices for each part and their coupling are provided in the next sections.

2.4. Elastic energy

The elastic energy is coupled with the concentration field in two ways. First, we have the decomposition of the strain tensor ($\boldsymbol{\varepsilon} = \boldsymbol{\varepsilon}_e + \boldsymbol{\varepsilon}_c$), and the second one can account for

concentration-dependent elastic properties (i.e. $\mathbb{C}(c)$). Furthermore, the stiffness tensor $\mathbb{C}$ is also under the influence of damage through a damage function $f_d(d)$. This damage function monolithically decreases from one to zero as the damage parameter increases from zero to one. In other words, the bulk elastic energy density vanishes at the crack surface (i.e. when $d \to 1.0$) and remains intact when $d = 0$. The elastic energy is thus given by:

$$\psi_e = \frac{1}{2}\,\boldsymbol{\varepsilon}_e : \mathbb{C}(c,d) : \boldsymbol{\varepsilon}_e = \frac{1}{2}\,(\boldsymbol{\varepsilon} - \boldsymbol{\varepsilon}_c) : \mathbb{C} : (\boldsymbol{\varepsilon} - \boldsymbol{\varepsilon}_c). \tag{6}$$

The material should not undergo crack evolution during compressive forces. Therefore, the expression for the damaged elastic stiffness tensor is split into two parts [35]

$$\mathbb{C}(c,d) = f_d\;\mathbb{C}_0(c) + (1 - f_d)\mathbb{P}. \tag{7}$$

Here, $\mathbb{C}_0 = \lambda \boldsymbol{I} \otimes \boldsymbol{I} + 2\mu\mathbb{I}^s$ is the 4th order tensor and $\mathbb{C}$ is the 4th order damaged elasticity tensor. In this method, the compressive regime is determined based on the trace of strain tensor (i.e. $\mathrm{tr}(\boldsymbol{\varepsilon})$). Therefore, the projection tensor $\mathbb{P}$ is defined according to

$$\mathbb{P} = k_0\;\mathrm{sgn}^-(\mathrm{tr}(\boldsymbol{\varepsilon}_e))\;\boldsymbol{I} \otimes \boldsymbol{I}, \tag{8}$$

$$\mathbb{C}_h = \mathbb{C}_0 - \mathbb{P}. \tag{9}$$

Here $\mathbb{P}$ and $\mathbb{C}_h$ are also 4th order tensors and $\mathrm{sgn}^-(\bullet) = (\bullet - |\bullet|)/2(\bullet)$. Moreover, $(\mathbb{I}^s)_{ijkl} = \frac{1}{2}(\delta_{ik}\delta_{jl} + \delta_{il}\delta_{jk})$ is the symmetric fourth-order identity tensor. The second order identity tensor is defined as $(\boldsymbol{I})_{ij} = \delta_{ij}$. The bulk modulus of the material is defined as $k_0 = \lambda + \frac{2}{3}\,\mu$. Considering Young's Modulus E and the Poisson ratio ν for elastic isotropic materials, $\lambda = \dfrac{E\nu}{(1+\nu)(1-2\nu)}$ and $\mu = G = \dfrac{E}{2(1+\nu)}$ are the Lame constants. There are other developments to take into account the so-called tension-compression asymmetry in the context of damage mechanics. Interested readers are also referred to [36].

Finally, the damage function is defined as:

$$f_d(d) = \frac{(1-d)^2}{(1-d)^2 + a_1 d(1 + a_2 d)}, \quad a_1 = \frac{4EG_c}{\pi l_c \sigma_u^2}, \quad a_2 = -0.5. \tag{10}$$

In the above relations, a rational degradation function is introduced to use the phase-field regularised cohesive zone model [45]. This is also known as the cohesive phase-field model (CPF) which is shown to be insensitive with respect to the internal length scale parameter in purely mechanical and thermomechanical scenarios. [75, 47]. This is unlike standard phase-field damage models (SPF) with a quadratic degradation function where the length scale parameter influences the strength of the material. Such features are achieved by taking into account the strength of the material σ_u as an additional material parameter in the model as well as introducing a threshold value for damage initiation. See also similar studies on cohesive fracture [46, 42, 47] as well as the summary provided in Table 2. Further explanations on the advantage of this CPF over SPF are provided in [47, 75] and what follows.

Remark 1. Note that in general elastic and fracture properties may be concentration-dependent. In other words, we have $E(c), G_c(c)$ and $\sigma_u(c)$. In this work, we mainly focus on fracture properties and therefore the elastic properties remain concentration-independent. Moreover, utilizing the cohesive PF approach, the results of the formulation converge by choosing a small enough length scale parameter. In other words, the internal length scale will not influence the physical response of the system and therefore one has better control over the crack initiation. Moreover, the damage zone is limited and fewer spread thanks to the additional threshold value.

2.5. Chemical Energy

The chemical energy as a result of the presence of chemical species (e.g. Lithium ions) within the bulk of the material is given by:

$$\psi_c = \; RTc_{max}[\tilde{c}\,\ln\tilde{c} + (1-\tilde{c})\,\ln(1-\tilde{c})] + RTc_{max}\chi\tilde{c}\,(1-\tilde{c}) + \frac{1}{2}c_{max}\kappa\nabla\tilde{c}\cdot\nabla\tilde{c}. \tag{11}$$

Here, $\tilde{c} = c/c_{\max}$ is the normalised concentration, R is the gas constant, T is the reference temperature and κ is an interphase parameter. The first term in Eq. 11 represents the entropic contribution to the system and the second term stands for the enthalpic contribution which favors the separation of the system. One can investigate the single-phase system by setting $\chi < 2$, while $\chi > 2$ is adopted for the coexistence of the two-phase system [76, 77]. The scalar parameter κ denotes the interface energy parameter. See also [78] for similar studies.

Remark 2. A possible coupling between the damage and concentration field is by multiplying the chemical energy with the damage function. As we will show later, by doing so, the damage driving force becomes overly complicated. Instead, we intend to keep chemical energy to be damage-independent and make the chemical flux to be damage-dependent.

2.6. Damage Energy

In the smeared approaches for fracture like PF damage models, the (sharp) crack surfaces in the bulk are replaced with a diffusive damage zone. Therefore, the fracture energy will be dissipated via crack density function γ within the volume as follows [36, 45, 47]:

$$\psi_d = G_c(c)\;\gamma(d,\nabla d) = \frac{G_c}{w_0}\left(\frac{1}{l_c}\omega(d) + l_c\;\nabla d\cdot\boldsymbol{A}\cdot\nabla d\right). \tag{12}$$

Here, $\omega(d) = 2d - d^2$ is the crack geometric function and the internal length scale parameter is denoted by l_c. The constant scaling parameter $w_0 = 4\int_0^1 \sqrt{\omega(d)}\;\mathrm{d}d = \pi$ is obtained to make sure that the dissipated energy per volume remains equal to the material fracture energy parameter G_c. Finally, the second-order structural tensor $\boldsymbol{A} = \boldsymbol{I} + \alpha\;\boldsymbol{a}\otimes\boldsymbol{a}$ is constructed based on the vector $\boldsymbol{a} = [\cos(\phi)\;\sin(\phi)]^T$. Utilizing a non-zero value for the parameter α, one can penalize the crack direction along the angle ϕ [47]. The angle ϕ is treated as a constant input parameter and it is in accordance with the preferential crack direction.

Remark 3. There are various choices for the damage function f_d [79]. Here we compare two mainstreams known as the AT2 phase-field damage model with quadratic degradation function (see e.g. [36]) against the cohesive phase-field model (see e.g. [45]). In Table 2, one can also see a simple receipt to switch between the two formulations. Note that the chosen relation and value for a_1 and a_2 results in a bilinear cohesive behavior as the damage variable evolves within the localized zone [45]. It is worth mentioning that the latter developments are limited to mode I fracture and mainly isotropic settings for fracture.

Remark 4. In this work, we tend to keep a_1 parameter concentration independent. To do so, one can use specific relation for $G_c(c)$ and $\sigma_u(c)$ so that this ratio holds $G_c(c)/\sigma_u^2(c) = \text{cte}$. This assumption leads to a constant value for the parameter a_1 and therefore the whole expression for the degradation function f_d is concentration-independent. From this assumption, we simplify the derivation of the model. Nevertheless, one can also consider concentration-dependent f_d upon having reliable experimental evidence. This will not result in any change within the current framework and simply more additional coupling terms will come into the final picture (see also [75]).

2.7. Thermodynamic forces

At this point, all the terms in Eq. 5 are defined according to the relations through Eqs. 6,11 and 12. Therefore, the time derivative of the total internal energy gives us

$$\dot{\psi} = \frac{\partial \psi}{\partial \boldsymbol{\varepsilon}} : \dot{\boldsymbol{\varepsilon}} + \frac{\partial \psi}{\partial c}\dot{c} + \frac{\partial \psi}{\partial \nabla c} \cdot \dot{\nabla} c + \frac{\partial \psi}{\partial d}\dot{d} + \frac{\partial \psi}{\partial \nabla d}\dot{\nabla} d. \tag{13}$$

As mentioned before, for the described chemo-mechanical coupled system, the first and second law of thermodynamics is elaborated in Appendix A which resulted in the simplified local version of the dissipation inequality (see Eq. 4). By plugging in the time derivative of free energy formation Eq. 13 into Eq. 4, the local dissipation inequality is written as:

$$\begin{aligned} \boldsymbol{\sigma} : \dot{\boldsymbol{\varepsilon}} - \left(\frac{\partial \psi}{\partial \varepsilon} : \dot{\boldsymbol{\varepsilon}} + \frac{\partial \psi}{\partial c}\dot{c} + \frac{\partial \psi}{\partial \nabla c} \cdot \dot{\nabla} c + \frac{\partial \psi}{\partial d}\dot{d} + \frac{\partial \psi}{\partial \nabla d}\dot{\nabla} d \right) \\ + \left(\nabla \cdot \boldsymbol{\zeta}\right) \dot{c} + \boldsymbol{\zeta} \cdot \dot{\nabla} c + \mu \dot{c} - \boldsymbol{J} \cdot \nabla \mu + Y \dot{d} + \boldsymbol{H} \cdot \dot{\nabla} d \geq 0. \end{aligned} \tag{14}$$

The above expression is then further simplified as

$$\begin{aligned} \left(\boldsymbol{\sigma} - \frac{\partial \psi}{\partial \boldsymbol{\varepsilon}} \right) : \dot{\boldsymbol{\varepsilon}} + \left(\mu_{net} - \frac{\partial \psi}{\partial c} \right) \dot{c} + \left(\boldsymbol{\zeta} - \frac{\partial \psi}{\partial \nabla c} \right) \dot{\nabla} c \\ + \left(Y - \frac{\partial \psi}{\partial d} \right) \dot{d} + \left(\boldsymbol{H} - \frac{\partial \psi}{\partial \nabla d} \right) \dot{\nabla} d - \boldsymbol{J} \cdot \nabla \mu \geq 0, \end{aligned} \tag{15}$$

where, μ_{net} is defined as $\mu_{net} = \mu + \nabla \cdot \boldsymbol{\zeta}$. To satisfy the dissipation inequality for an arbitrary process, one possible approach is [63, 3]:

$$\boldsymbol{\sigma} = \frac{\partial \psi}{\partial \boldsymbol{\varepsilon}} = \frac{\partial \psi_e}{\partial \boldsymbol{\varepsilon}} = \mathbb{C}(c,d) : (\boldsymbol{\varepsilon} - \boldsymbol{\varepsilon}_c) = \ \mathbb{C}(c,d) : \boldsymbol{\varepsilon}_e, \tag{16}$$

$$\boldsymbol{\zeta} = \frac{\partial \psi}{\partial \nabla c} = \kappa c_{max} |\nabla \tilde{c}|. \tag{17}$$

$$\mu = \frac{\partial \psi}{\partial c} - \nabla \cdot \boldsymbol{\zeta} = RT \left(\ln \frac{\tilde{c}}{1-\tilde{c}} + \chi(1-2\tilde{c}) \right) - \kappa c_{max} |\nabla^2 \tilde{c}| + \frac{1}{2}\ \boldsymbol{\varepsilon}_e : \frac{\partial \mathbb{C}}{\partial c} : \boldsymbol{\varepsilon}_e - \boldsymbol{\sigma} : \boldsymbol{\Omega} + \gamma \frac{\mathrm{d}G_c(c)}{\mathrm{d}c}, \tag{18}$$

$$Y = \frac{\partial \psi}{\partial d} = \frac{\partial (\psi_e + \psi_d)}{\partial d} = \frac{1}{2}\ \boldsymbol{\varepsilon}_e : \frac{\partial \mathbb{C}}{\partial d} : \boldsymbol{\varepsilon}_e + G_c(c) \frac{\omega'(d)}{\pi l_c}, \tag{19}$$

$$\boldsymbol{H} = \frac{\partial \psi}{\partial \nabla d} = \frac{\partial \psi_d}{\partial \nabla d} = \frac{2}{\pi} G_c(c)\ l_c \nabla d. \tag{20}$$

Note that based on the above derivation, the chemical potential (Eq. 18) is enhanced by the stress tensor as well as the derivation of the fracture energy with respect to the concentration variable. The remaining term in the dissipation inequality reads

$$-\boldsymbol{J} \cdot \nabla \mu \geq 0. \tag{21}$$

To ensure non-negative dissipation, the flux vector is obtained via the potential Φ^c:

$$\Phi^c = \frac{1}{2} M(c,d) ||\nabla \mu||^2. \tag{22}$$

We assumed isotropic concentration-dependent mobility parameter M according to

$$M(c,d) = h_d(d) M_0(c) = h_d(d) \frac{D}{RT}\ c\ (1-\tilde{c}). \tag{23}$$

Here D is the diffusivities inside the bulk. To degrade the chemical flux, we utilized the chemical damage function $h_d(d) = f_d(d)$ which takes the same formula as the mechanical damage function. Note that one can also investigate other choices such as $h_d = (1-d)^b$ where b is a constant positive real number. Assuming concentration-independent elastic properties, the flux vectors within the bulk and the interface are then obtained as:

$$\begin{aligned} \boldsymbol{J} &= -M(c,d) \nabla \mu = \\ &- h_d(d) M_0(c) \nabla \left(RT \left(\ln \frac{\tilde{c}}{1-\tilde{c}} + \chi(1-2\tilde{c}) \right) - \kappa c_{max} |\nabla^2 \tilde{c}| - \ \boldsymbol{\sigma} : \boldsymbol{\Omega} + \gamma \frac{\mathrm{d}G_c(c)}{\mathrm{d}c} \right). \end{aligned} \tag{24}$$

From the numerical point of view and based on the consistent derivation, the last term in Eq. 24 appears in the flux vector. From the physical point of view, this term represents additional flux in regions where $\gamma \neq 0$ (i.e. transition from undamaged to damaged regions). We will study this matter further in the numerical examples.

Remark 4. The function $h_d(d)$ in Eq. 23, similar to the damage function for elastic energy f_d, decreases monolithically as the damage parameter increase from zero to one. As

a result, the species flux will be cut off at the freshly created crack surfaces. Such coupling becomes essential as it will be shown in the numerical examples (see also [80] for the same effect in thermally induced fracture). For future developments, one can consider anisotropic damage growth [47] or consider the influence of mode-mixity on the flux vector [3].

Remark 5. Note that in the application of batteries, the stability of the material may increase upon lithiation. For example when it comes to lithiation in the cathode active material like lithium nickel manganese cobalt oxides, $LiNi_xMn_yCo_zO_2$ (NMC) or lithium cobalt oxide $LiCoO_2$, Lithium atoms fill-up the nanovoids and result in a tougher material behavior [16]. On the other hand, could be that the material becomes brittle upon the increase in the chemical concentration (Li-embrittlement) [3]. This case is particularly interesting when the cathode active material goes under delithiation.

2.8. Summary of governing equations

A summary of governing equations for displacement, concentration, as well as damage field, is provided in Table 1. It is worth mentioning that for the displacement and damage field one can apply the Euler-Lagrange procedure or variational derivative with respect to $\boldsymbol{u}$ and d to obtain the relative differential equation for displacement and damage, respectively. The latter is also similar to the Allen-Chan evolution equation (see also [37]). When it comes to the concentration field c, the Chan-Hillirad procedure should be applied to satisfy the conservation of mass [55, 76]. Here we define $\mu_{net} = RT\left(\ln\frac{\tilde{c}}{1-\tilde{c}} + \chi(1-2\tilde{c})\right) - \boldsymbol{\sigma} : \boldsymbol{\Omega} + \gamma\frac{dG_c}{dc}$ and the elastic properties are assumed to be independent of the concentration field.

Displacement	Concentration	Damage
$\nabla \cdot \boldsymbol{\sigma} + \boldsymbol{b} = 0$	$\nabla \cdot \boldsymbol{J} + \dot{c} = 0$	$\nabla \cdot \boldsymbol{H} + Y = 0$
$\boldsymbol{\sigma} = \mathbb{C}(d) : \boldsymbol{\varepsilon}_e$	$\boldsymbol{J} = -M(c,d)\ \nabla\mu$	$\boldsymbol{H} = \frac{2l_c}{\pi} G_c(c)\nabla d$
$\boldsymbol{\varepsilon}_e = \boldsymbol{\varepsilon} - (c-c_0)\ \boldsymbol{\Omega}$	$\mu = \mu_{net} - \nabla \cdot \boldsymbol{\zeta}$	$Y = -f_d'\mathcal{H} - \omega'\frac{G_c}{\pi l_c}$

Table 1: chemo-mechanical coupled formulation of cohesive fracture.

In Table 1, the expression for $\mathcal{H}$ is defined as the maximum value between the undamaged elastic strain through the simulation time $\psi_e^0(t) = \frac{1}{2}\ \boldsymbol{\varepsilon}_e : \mathbb{C}_h : \boldsymbol{\varepsilon}_e$, and the damage energy threshold $\psi_{th} = \frac{1}{2E}\ \sigma_u^2$ [47]:

$$\mathcal{H} = \max_t(\psi_e^0(t), \psi_{th}). \tag{25}$$

This history parameter assures damage irreversibility condition upon unloading the system and therefore it is essential for cyclic loading (e.g. lithiation and delithation cycles). In Table 2 a comparison is made between the AT2 and cohesive PF fracture model.

The boundary conditions for different fields are summarized in Eq. 26. Here, the external traction $\boldsymbol{t}_p$ and the displacement boundary condition $\boldsymbol{u}_p$ are applied along ∂V_t and ∂V_u,

	AT2 PF model	Cohesive PF model
Crack topology function	$\omega(d) = d^2$, $w_0 = 2$	$\omega(d) = 2d - d^2$, $w_0 = \pi$
Damage function	$f_d = (1-d)^2$	$f_d = \dfrac{(1-d)^2}{(1-d)^2 + a_1 d + a_1 a_2 d^2}$
History parameter	$\mathcal{H} = \max_t(\psi_e^0(t))$	$\mathcal{H} = \max_t(\psi_e^0(t), \dfrac{\sigma_u^2}{2E})$

Table 2: Standard versus cohesive phase-field damage models.

respectively. The external flux $\boldsymbol{J}_p$ and the concentration boundary condition c_p are applied along ∂V_J and ∂V_c, respectively. Note that for the damage field, the only required boundary condition reads as $\nabla d \cdot \boldsymbol{n} = 0$ on external boundaries (i.e. ∂V).

$$\left\{ \begin{array}{ll} \boldsymbol{u} = \boldsymbol{u}_p & \text{on } \partial V_u \\ \boldsymbol{\sigma} \cdot \boldsymbol{n} = \boldsymbol{t}_p & \text{on } \partial V_t \end{array} \right. , \quad \left\{ \begin{array}{ll} c = c_p & \text{on } \partial V_c \\ \boldsymbol{J} \cdot \boldsymbol{n} = J_p & \text{on } \partial V_J \end{array} \right. \tag{26}$$

Apart from the bulk model, the electrochemical reaction equation should be addressed as well. The electrostatic and electrochemical potential at the interface between the AM and the SE determines how the Lithium ions in the solid electrolytes (SE) are transported. The latter can be described via a Faradaic reaction, i.e. $\mathrm{Li}^+ + e^- \rightleftharpoons \mathrm{Li}$. The resultant neutral Lithium moves in the host material according to the diffusion mechanism. It is known that losing bonding or contact at the interface between SE and AM hinders the aforementioned chemical reaction. The rate of the reaction on the interface between the AM and SE is described by the phenomenological Butler-Volmer (BV) equation [81, 82, 83, 84]

$$j_s = c_{\text{surf}} \frac{a_+^{1-\beta} a^{\beta}}{\tau_0 \gamma_A} \left[\exp\left(-\beta \frac{F\eta}{RT} \right) - \exp\left((1-\beta) \frac{F\eta}{RT} \right) \right], \tag{27}$$

where c_{surf} is the molar concentration of intercalation sites on the surface, τ_0 represents the meantime for a single reaction step. The parameter $\gamma_A = (1-c)^{-1}$ denotes the chemical activity coefficient of the activated state, while $\beta = 0.5$ is the transfer coefficient for forward and backward reactions. The Faraday constant F describes the amount of electric charge of one mole of electrons [55]. Finally, the quantities a, a^+, and a^- are the activities of Li, Li^+, and the electron, respectively. Following the similar approach described in [55], the BV relation in Eq. 27 is rewritten as:

$$j_s = (1-D) \left[\frac{c_{\text{surf}}}{\tau_0} (1-\tilde{c}) \exp\left(-\frac{F}{2RT} \Delta\phi \right) - \frac{c_{\text{surf}}}{\tau_0} (1-\tilde{c}) \exp\left(\frac{\mu}{RT} + \frac{F}{2RT} \Delta\phi \right) \right], \tag{28}$$

where $\Delta\phi = \phi_e - \phi$ is the voltage drop across the interface, and μ is the chemical potential of the active material in contact with the electrolyte. Note that in Eq. 28, the parameter D denoted the damage from CZ elements. This damage parameter is determined based on the given displacement jump at the interface [3]. In future developments, the current cohesive PF model can be extended to take into account the electrochemical reaction and as a result, the model can be also used for interphase between AM and SE.

3. Finite element implementation

In this part, we drive the weak form for the different involved physics in the problem considering the governing equations summarized in Table 1. This is achieved by multiplying the mechanical, chemical concentration, chemical potential and damage governing equation by a virtual displacement field $\delta\boldsymbol{u}$, chemical concentration field δc, chemical potential field $\delta\mu$ and damage field δd, respectively. By applying integration by part, Gauss' theorem, and considering standard boundary conditions we have:

$$\int_V (\nabla\cdot\boldsymbol{\sigma}+\boldsymbol{b})\ \delta\boldsymbol{u}\ dV = \int_{\partial V}\boldsymbol{t}\cdot\delta\boldsymbol{u}\ dS - \int_V \boldsymbol{\sigma}:\delta\boldsymbol{\varepsilon}\ dV + \int_V \boldsymbol{b}\cdot\delta\boldsymbol{u}\ dV, \tag{29}$$

$$\int_V (\nabla\cdot\boldsymbol{J}+\dot{c})\ \delta c\ dV = \int_{\partial V}\boldsymbol{J}\cdot\boldsymbol{n}\ \delta c\ dS\ - \int_V \boldsymbol{J}\ \nabla\delta c\ dV\ + \int_V \dot{c}\ \delta c\ dV, \tag{30}$$

$$\int_V (\nabla\cdot\boldsymbol{\zeta}+\mu-\mu_{net})\delta\mu\ dV = \int_{\partial V}\boldsymbol{\zeta}\cdot\boldsymbol{n}\ \delta\mu\ dS\ - \int_V \boldsymbol{\zeta}\ \nabla\delta\mu\ dV\ + \int_V (\mu-\mu_{net})\,\delta\mu\ dV, \tag{31}$$

$$\int_V (\nabla\cdot\boldsymbol{H}-Y)\ \delta d\ dV = \int_{\partial V}\boldsymbol{H}\cdot\boldsymbol{n}\ \delta d\ dS\ - \int_V \boldsymbol{H}\ \delta\nabla d\ dV\ - \int_V Y\ \delta d\ dV. \tag{32}$$

The above relations are discretized using the following approximations for the displacement, concentration, chemical potential and damage field as well as their spatial derivatives:

$$\begin{cases} \boldsymbol{u}=\boldsymbol{N}_u\boldsymbol{u}_e \\ \tilde{\boldsymbol{\varepsilon}}=\boldsymbol{B}_u\boldsymbol{u}_e \end{cases}, \quad \begin{cases} c=\boldsymbol{N}_c\boldsymbol{c}_e \\ \nabla c=\boldsymbol{B}_c\boldsymbol{c}_e \end{cases}, \quad \begin{cases} \mu=\boldsymbol{N}_\mu\boldsymbol{\mu}_e \\ \nabla\mu=\boldsymbol{B}_\mu\boldsymbol{\mu}_e \end{cases}, \quad \begin{cases} d=\boldsymbol{N}_d\boldsymbol{d}_e \\ \nabla d=\boldsymbol{B}_d\boldsymbol{d}_e \end{cases}. \tag{33}$$

In the above equation, $\boldsymbol{u}_e$, $\boldsymbol{c}_e$, $\boldsymbol{\mu}_e$ and $\boldsymbol{d}_e$ are the nodal values of displacement, concentration, chemical potential and damage values. Furthermore, $\tilde{\boldsymbol{\varepsilon}}$ is the strain in the Voigt notation. For a 2D quadrilateral linear element with four nodes, shape function matrices $\boldsymbol{N}_u$, $\boldsymbol{N}_c$, $\boldsymbol{N}_\mu$ and $\boldsymbol{N}_d$ and their first derivative $\boldsymbol{B}_u$, $\boldsymbol{B}_c$, $\boldsymbol{B}_\mu$ and $\boldsymbol{B}_d$ are introduced below:

$$\boldsymbol{N}_u=\begin{bmatrix} N_1 & 0 & \dots & N_4 & 0 \\ 0 & N_1 & \dots & 0 & N_4 \end{bmatrix},\ \boldsymbol{N}_c=\boldsymbol{N}_\mu=\boldsymbol{N}_d=\begin{bmatrix} N_1 & \dots & N_4 \end{bmatrix}. \tag{34}$$

$$\boldsymbol{B}_u=\begin{bmatrix} N_{1,x} & 0 & \dots & N_{4,x} & 0 \\ 0 & N_{1,y} & \dots & 0 & N_{4,y} \\ N_{1,y} & N_{1,x} & \dots & N_{4,y} & N_{4,x} \end{bmatrix},\ \boldsymbol{B}_c=\boldsymbol{B}_\mu=\boldsymbol{B}_d=\begin{bmatrix} N_{1,x} & \dots & N_{4,x} \\ N_{1,y} & \dots & N_{4,y} \end{bmatrix}. \tag{35}$$

The problem domain, V, is discretized into n_e number of elements (i.e. $V=\sum_{e=1}^{n_e}V_e$). The same holds for the boundary of the domain which is divided into n_b number of elements (i.e. $\partial V=\sum_{e=1}^{n_b}\partial V^e$). Inserting the above discretization relations into Eqs. 29 to 32, one

obtains all the residual vectors, for an arbitrary element V_e:

$$\boldsymbol{r}_u = \int_{\partial V_e} \boldsymbol{N}_u^T \ \boldsymbol{t} \ dS - \int_{V_e} \boldsymbol{B}_u^T \ \tilde{\boldsymbol{\sigma}} dV + \int_{V_e} \boldsymbol{N}_u^T \ \boldsymbol{b} \ dV, \tag{36}$$

$$\boldsymbol{r}_c = \int_{\partial V_e} \boldsymbol{N}_c^T (\boldsymbol{J} \cdot \boldsymbol{n}) \ dS \ - \int_{V_e} \boldsymbol{B}_c^T \boldsymbol{J} \ dV + \int_{V_e} \boldsymbol{N}_c^T \ \dot{c} \ dV, \tag{37}$$

$$\boldsymbol{r}_\mu = \int_{\partial V_e} \boldsymbol{N}_c^T (\boldsymbol{\zeta} \cdot \boldsymbol{n}) \ dS \ - \int_{V_e} \boldsymbol{B}_\mu^T \boldsymbol{\zeta} \ dV + \int_{V_e} \boldsymbol{N}_\mu^T \ (\mu - \mu_{net}) \ dV, \tag{38}$$

$$\boldsymbol{r}_d = \int_{\partial V_e} \boldsymbol{N}_d^T (\boldsymbol{H} \cdot \boldsymbol{n}) \ dS - \int_{V_e} (\boldsymbol{B}_d^T \ \boldsymbol{H}) \ dV - \int_{V_e} \boldsymbol{N}_d^T \ Y \ dV. \tag{39}$$

In Eq. 36, $\tilde{\boldsymbol{\sigma}}$ is the stress tensor in Voigt notation. Furthermore, the time discretization is performed by dividing the total time by n_t time steps of the size Δt. Therefore the term $\dot{c}$ in Eq. 37 can be written $\dot{c} = \dfrac{c^{n+1} - c^n}{\Delta t}$. The known value c^n is the concentration in the previous time step, and the unknown value c^{n+1} is the concentration related to the current time step. Finally, the gradient of the hydrostatic stress $\nabla \boldsymbol{\sigma}_h$ (see Eq. 37), is calculated by multiplying its nodal values by the gradient of shape functions $\boldsymbol{B}_u$. The hydrostatic stress $\boldsymbol{\sigma}_h$ is calculated at each integration point from the nodal displacement values $\boldsymbol{u}$. It is then extrapolated to the nodes using the shape functions matrix. In this approach, there is no need for higher-order shape functions [3, 75].

The introduced model is implemented into the open-source FEM framework Multiphysics Object-Oriented Simulation Environment (MOOSE) [85, 86]. The coupled sets of PDEs of the bulk element are solved by PETSc [87] (see also [63, 3]). Moreover, our initial implementation for the damage model is based on the RACCOON framework which is an application in the MOOSE platform to model the fracture of materials using the phase-field approach [88, 89]. We further developed existing codes according to our needs and what is described in the previous section for the introduced model. Such implementations are also available for interested readers upon their request. The geometry for different structures in this work is designed and meshed with the aid of the open-source software Gmsh 4.8 [90]. Finally, the data analysis, visualization, and representation are carried out on ParaView 5.9 [91].

Non-linear systems of equations are usually solved by applying Newton Raphson's method for which one requires derivation and construction of the Jacobian matrix (derivation of residuals with respect to the degrees of freedom). Computing the latter matrices is a tedious task in numerical computations. On the other hand, one can take advantage of the methods such as automatic differentiation (AD) [92]. In this study, AD is employed in the implementation of codes related to chemo-mechanics and phase-field fracture to simplify the process of implementation and to guarantee accurate results without errors arising from truncating derivatives in the manual construction of the Jacobian. The Multi-app approach [93] is used which allows a straight way for coupling different physics in the MOOSE platform.

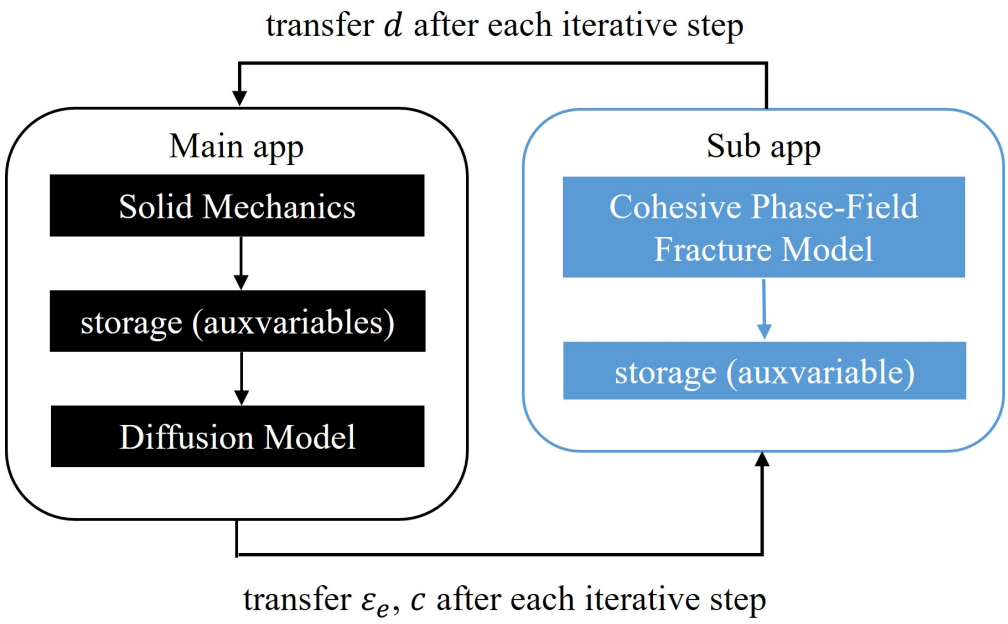

Figure 3: Connection between modules coded in the FE program MOOSE.

As seen in Fig. 3, the multi-app is run with a main/master app and a sub-app. A master app in which most processes are run is established and from which other sub-apps are called to solve different physics of the whole problems. In this study, the chemical and mechanical parts of the implementation are written in one input file and fully coupled as the master app. The damage residual is solved in a second input file (shown as the sub-app). The latter part is then called after every iteration in the master app in a staggered manner until convergence is reached. Relative tolerance of 10^{-8} is defined in our studies.

4. Numerical examples

The numerical results are categorized in two main directions. First, we focus on some fundamental aspects of crack propagation in a chemo-mechanical coupled solid. We intend to show the performance of the introduced model and later on the importance of different coupling terms and their influence on the overall results. Next, the focus is on more practical examples where we look into cracking of the active material and a composite system of AM and SE. The specific cathode material under consideration is V_2O_5 and the relative material parameters and their numerical values for the current simulations are provided in Table 3 (see also [94]). For the solid electrolyte, we consider LiLaZrO (see Table 5). These numbers are kept constant throughout the simulations unless it is mentioned otherwise for some parameter studies. Also, note that some of the fracture properties have to be assumed for the sake of numerical calculations due to the lack of available data. Nevertheless, this does not change the modeling strategy and our qualitative conclusions.

	Unit	Value
Young's modulus E	[GPa]	43
Maximum concentration $c_{\max}$	[mol/m^3]	12400
Poisson's ratio ν	[-]	0.3
Partial molar volume Ω	[m^3/mol]	4.85×10^{-6}
Diffusivity D	[m^2/s]	5.4×10^{-15}
Interface parameter κ	[Jm^2/mol]	1.2×10^{-12}
Phase parameter χ	[-]	2.4
Ultimate stress at null concentration σ_{u0}	[GPa]	0.8
fracture Toughness at null concentration G_{c0}	[J/m^2]	1.54
Gas constant R	[J/(mol.K)]	8.314
Temperature T	[K]	298.15

Table 3: Parameters used in the numerical Studies taken from [63]. The values for fracture properties (G_{c0} and σ_{u0}) are from the primarily atomistic calculations and are still unpublished. These values are also changed in some of the reported numerical studies.

4.1. Tensile test in a chemo-mechanical coupled single notched specimen

The geometry and boundary conditions for the mechanical and chemical part of the problem are shown in Fig. 4. The initial concentration of $c_0 = 0.5\ c_{max}$ is assumed. All the surrounding edges are chemically isolated and the upper edge is pulled in the $y-$direction and fixed in the $x-$direction. As we apply the displacement, the reaction forces are measured.

For the rest of the studies, the following normalized values are utilized according to Table 4. In normalizing values and parameters, we choose a characteristic length $\lambda = 1\ \mu$m and a characteristic time $\tau = 100$ sec.

Normalized quantity	Formula	Normalized quantity	Formula
Reaction force component F^*	$F/RT\lambda^2 c_{max}$	Hyd. stress σ_h^*	σ_h/RTc_{max}
Concentration c^*	c/c_{max}	Flux value J^*	$J\tau/\lambda c_{max}$

Table 4: Normalized quantities utilized in the simulations

.

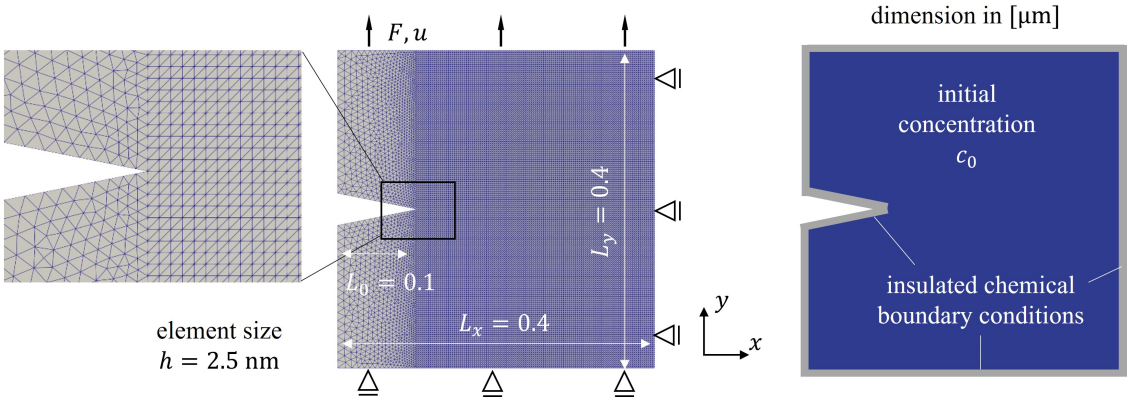

Figure 4: Meshed geometry and boundary conditions of a single notched specimen.

Fig. 5 shows the normalized reaction force component in the y direction for different values of l_c. One observes a convergence in the results as we decrease the value of l_c.

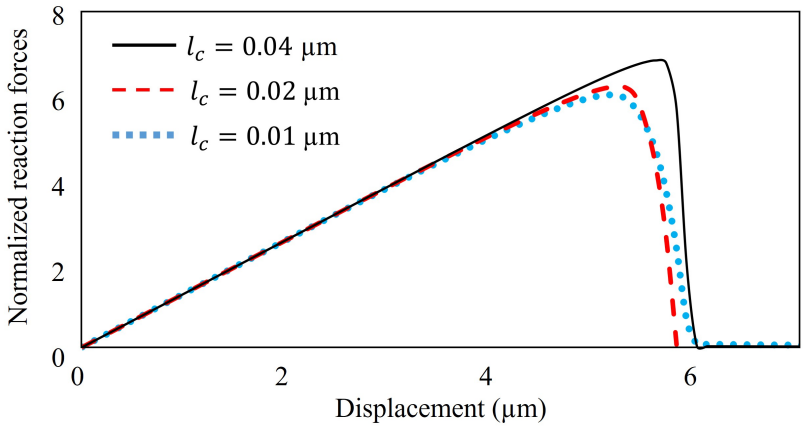

Figure 5: Convergence studies with respect to the internal length scale parameter l_c.

4.2. Dilithiation in a chemo-mechanical coupled single notched specimen

We now look into a case where the chemical flow drives the damage progression. The geometry and the boundary conditions are according to Fig. 6. The initial concentration of $c_0 = 0.9\ c_{max}$ is kept within the bulk. The concentration on the left edge is kept constant by applying a Dirichlet boundary condition ($c_{min} = 0.1\ c_{max}$). All other surfaces are insulated. Delithiation from the entire left-hand side of the sample is referred to as symmetric BCs while delithiation only from the top left-hand side is referred to as asymmetric BCs for what follows. Since in the symmetric delithiation example, species flux vectors are mainly parallel to the crack direction, the asymmetric delithiation is considered for a better study of the influence of the freshly created crack surface on the concentration profile.

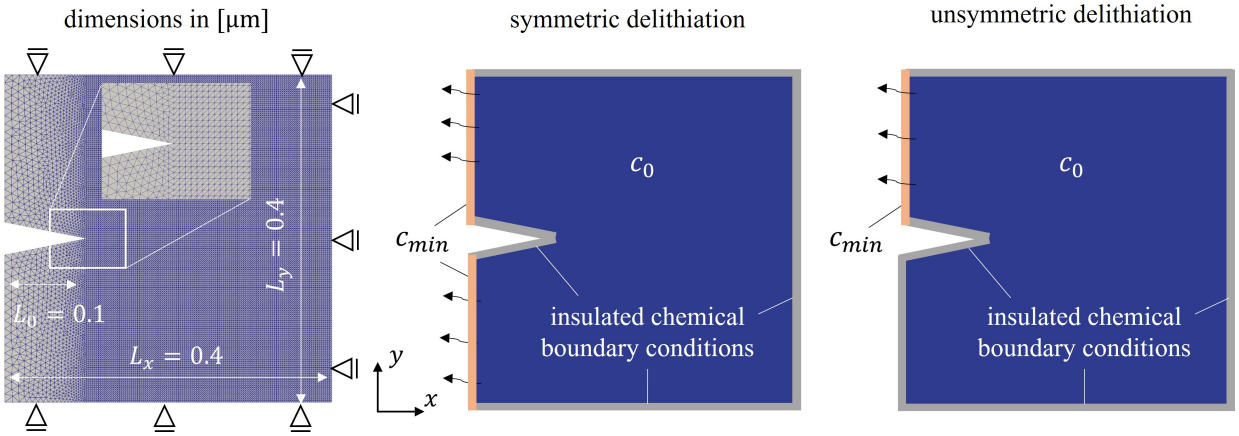

Figure 6: Meshed Geometry and boundary conditions of a single notched specimen.

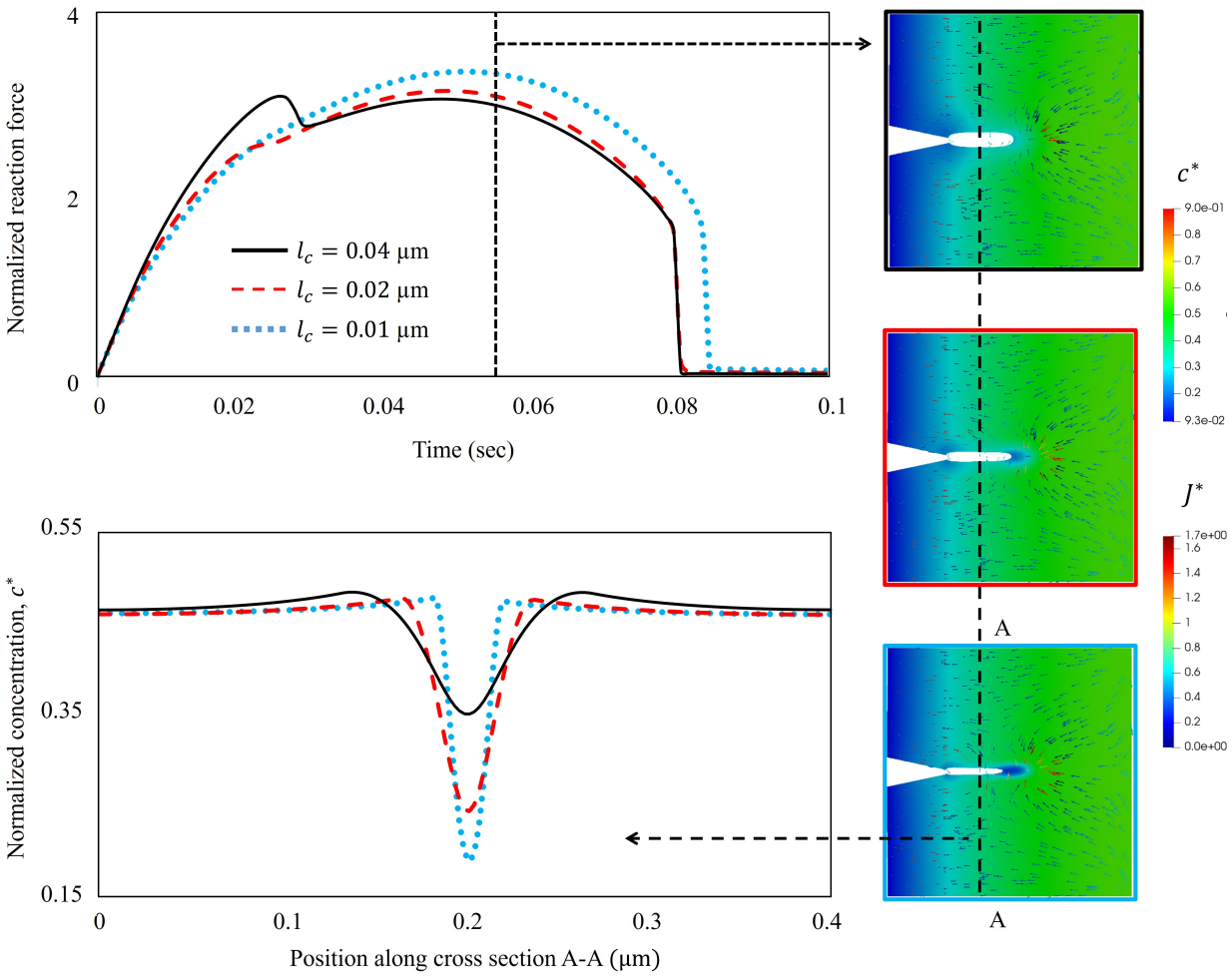

Figure 7: Convergence studies with respect to the internal length scale parameter l_c.

Here, we discuss the process of symmetric delithiation. As the lithium goes out, the whole specimen tends to shrink. Since the system is mechanically fixed at the top and bottom edges, it cannot shrink freely. As a result, tensile stresses develop within the material and the crack starts to propagate from the introduced initial notch. As more delithiation happens through time, the crack propagates further till the specimen is divided into two parts. Similar to the previous section, the reaction forces and concentration profile are compared for cases with different length scale parameters. Interestingly enough, again we observe a convergence behavior quantitatively and qualitatively in the obtained predictions. Moreover, for time $t = 0.055$ sec, the snapshots of the process are shown where the normalized concentration profile and the flux vector are plotted.

For a better comparison, the crack location is omitted for the region with damage higher than 0.8. The concentration profile is also plotted along the section $A - A$ which passes the damaged region. The results confirm the convergence of the predictions with respect to the length scale parameter. Certainly, one cannot choose an arbitrarily large value for l_c. Yet, by choosing small enough value for l_c and by including more physics into account the results are insensitive regarding the length scale parameter. The latter shows the model is much more reliable for critical predictions. These studies give us enough confidence to further explore other coupling terms in what follows.

For a better comparison, a summary of different models is provided below. Going from top to bottom (model A to D), more coupling terms between different active fields are considered.

What we presented for the length-scale studies is based on model C which takes into account many important features.

- Model A: we consider one-way coupling between mechanical and chemical parts ($\boldsymbol{\varepsilon} = \boldsymbol{\varepsilon}_e + \boldsymbol{\varepsilon}_c$). Diffusion depends solely on the concentration gradient (i.e. $\mu = \mu_0$). Mobility remains undamaged (i.e. $h_d(d) = 1$). Fracture properties remains constant (i.e. $G_c =$ cte. and $\sigma_u =$ cte.).

- Model B: We account for a two-way coupling between chemical and mechanical parts. In other words, in addition to $\boldsymbol{\varepsilon} = \boldsymbol{\varepsilon}_e + \boldsymbol{\varepsilon}_c$, stress is coupled with diffusion (i.e. $\mu = \mu_0 - \boldsymbol{\sigma} : \boldsymbol{\Omega}$). There is no direct coupling between concentration and damage fields. Mobility remains undamaged (i.e. $h_d(d) = 1$). Fracture properties remain constant (i.e. $G_c =$ cte. and $\sigma_u =$ cte.).

- Model C: We account for a two-way coupling between chemical and mechanical parts and a one-way coupling between concentration and damage field. Flux is under the influence of damage (i.e. $h_d(d) = f_d(d)$). Fracture properties remains constant (i.e. $G_c =$ cte. and $\sigma_u =$ cte.).

- Model D: We account for a two-way coupling between chemical and mechanical parts as well as a two-way coupling between concentration and damage fields. Flux is under the influence of damage (i.e. $h_d(d) = f_d(d)$). Fracture properties are concentration dependent (i.e. $G_c(c) = F(c)\ G_{c0}$, $\sigma_u(c) = \sqrt{F(c)}\ \sigma_{u0}$ and $\mu = \mu_0 - \boldsymbol{\sigma} : \boldsymbol{\Omega} + \gamma \dfrac{dG_c}{dc}$).

4.3. Influence of coupled hydrostatic stress

Utilizing the boundary value problem described in Fig. 6, a comparison is made between the formulation with hydrostatic stress uncoupled with diffusion and the one where stress is coupled with diffusion (see the definition for Model A and B). The results of such comparison in terms of the concentration profile, flux vector, hydrostatic stress as well as damaged regions are provided in Fig. 8.

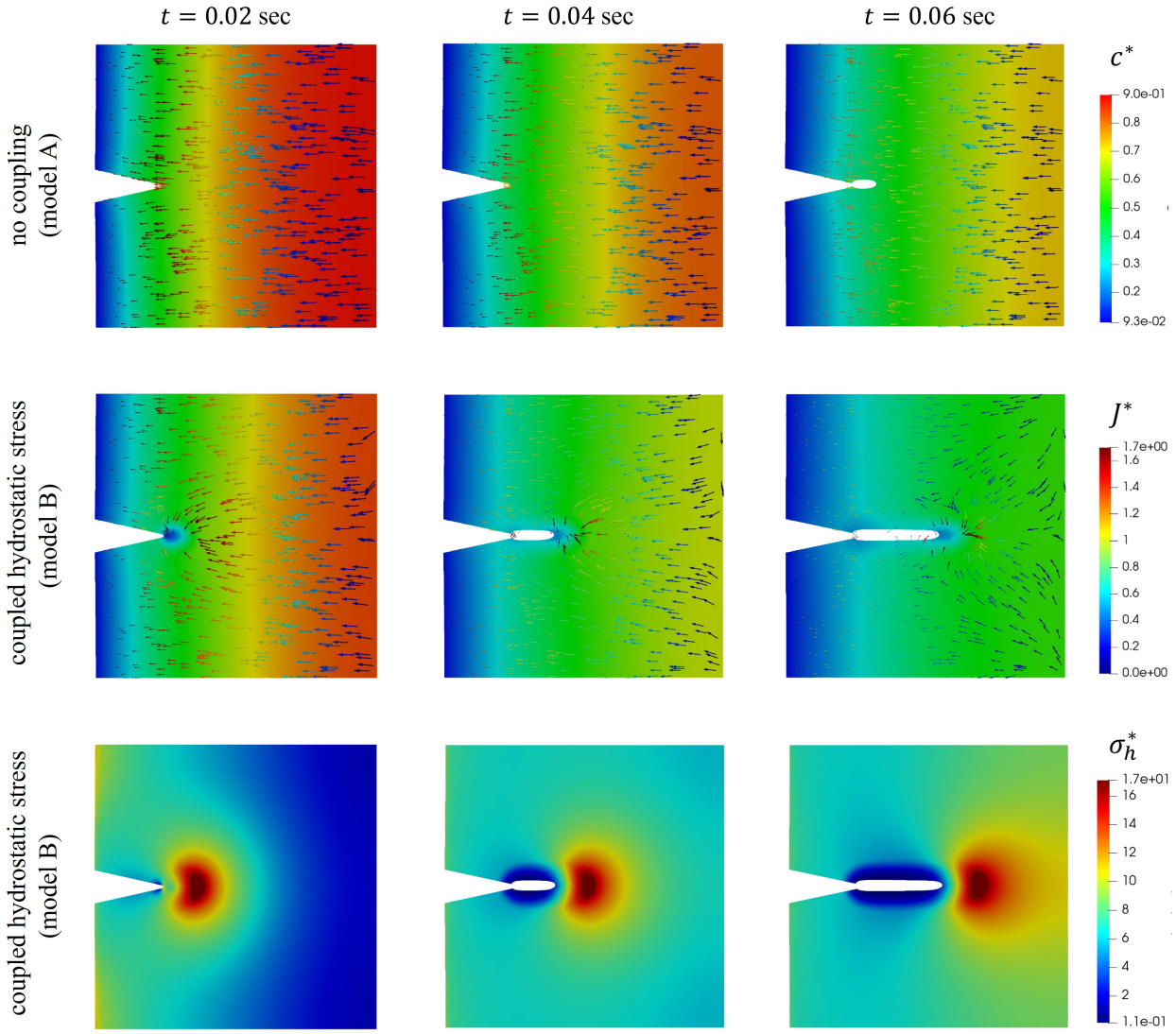

Figure 8: Comparison between uncoupled and coupled hydrostatic stress formulations (model A and B) utilizing symmetric delithation BCs.

First, we observe that the flux distribution is not homogeneous for model B. Here, the flux vector and concentration of chemical species are accumulated at the crack tip where we expect to have high tensile stresses (positive hydrostatic stress). This is in contrast to the almost homogeneous distribution of flux for model A where we have no strong coupling between the chemical and mechanical fields. Second, we observe that the crack propagation

initiation is different. One naturally expects that the accumulation of the concentration at the crack tip will locally increase the chemical strain and therefore reduce the elastic strain and relax the stress at the crack tip. Here we conclude that the latter point is not enough to judge the cracking propagation behavior. In this example, the other parts of the system which are away from the crack tip are under severe delithation. As a result, for model B, the whole specimen shrinks more which results in a higher driving force (elastic energy) for damage.

4.4. Cutting off the flux vector at freshly created crack surface

According to Eq. 24, we proposed to introduce the influence of the damage parameter on the flux vector by utilizing the damage function that decreases monolithically as the damage parameter increases from zero to one. This is considered in Model C. To properly study this effect, the BCs with asymmetric delithiation are considered (see also Fig. 6). In what follows, we compare the results of model C against those from model B.

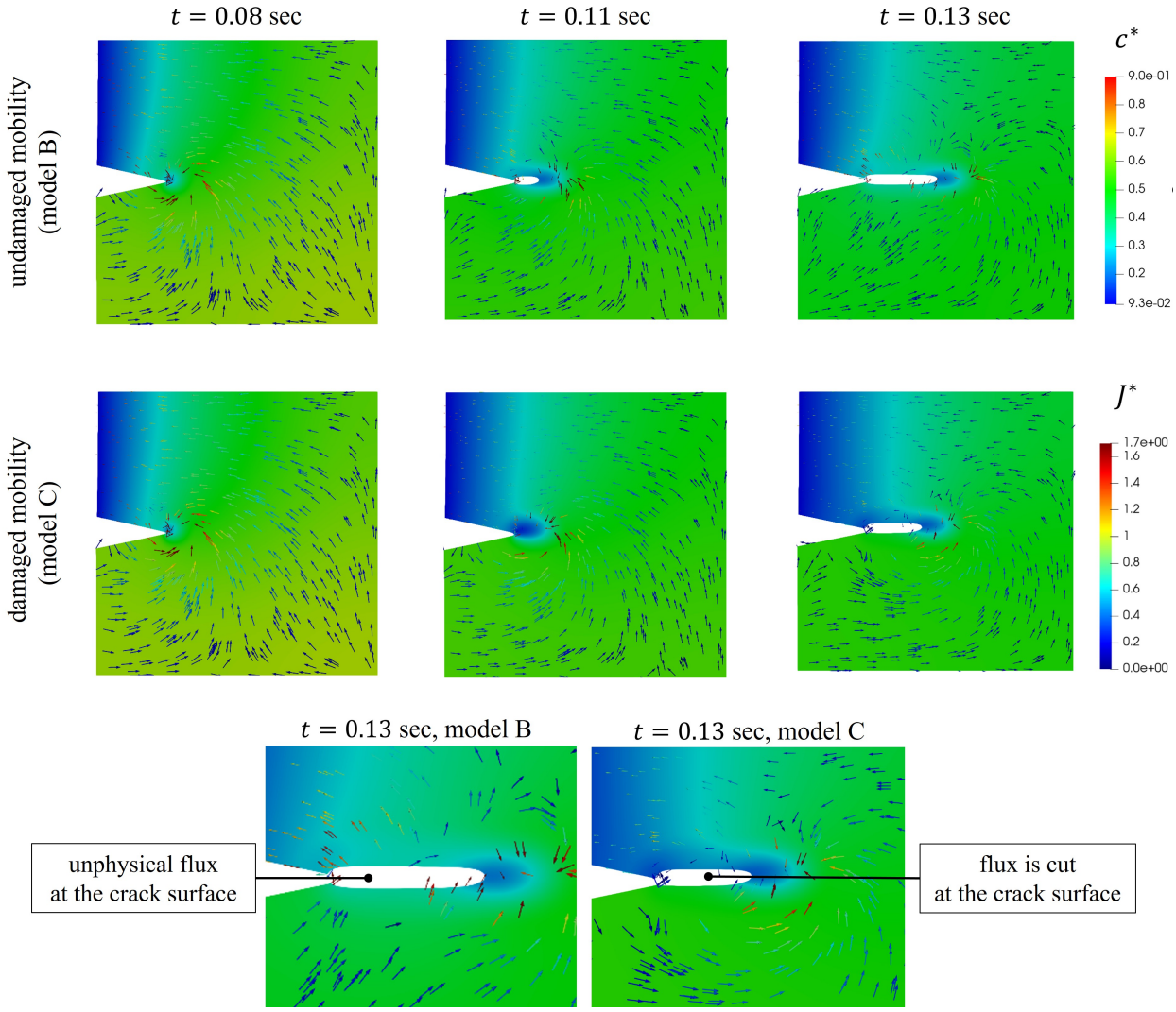

Figure 9: Comparison of damaged and undamaged mobility formulations (model B and C) utilizing unsymmetric delithation BCs.

Based on the results reported in Fig. 9, we conclude two major points. First, for model B, the flux vector is in accordance with the concentration gradient imposed for delithiation. Moreover, the flux vector from the lower section of the specimen goes directly through the cracked surface without respecting the presence of the freshly created damaged surfaces. The latter point is not physically accurate. On the other hand, the concentration profile for model C (where mobility is damaged) shows the flux circumventing the crack. Secondly, it is observed that there is a slight change in the crack propagation behavior which is associated with the faster delithiation for model B where concentration flux can pass through the crack surface resulting in an inaccurate crack propagation behavior.

4.5. Influence of concentration-dependent fracture properties

For the next study, fracture properties are assumed to depend on the concentration value. Therefore, properties such as damage onset and fracture energy are defined to be concentration-dependent. In battery systems, the latter is known as Li-embrittlement [16, 3].

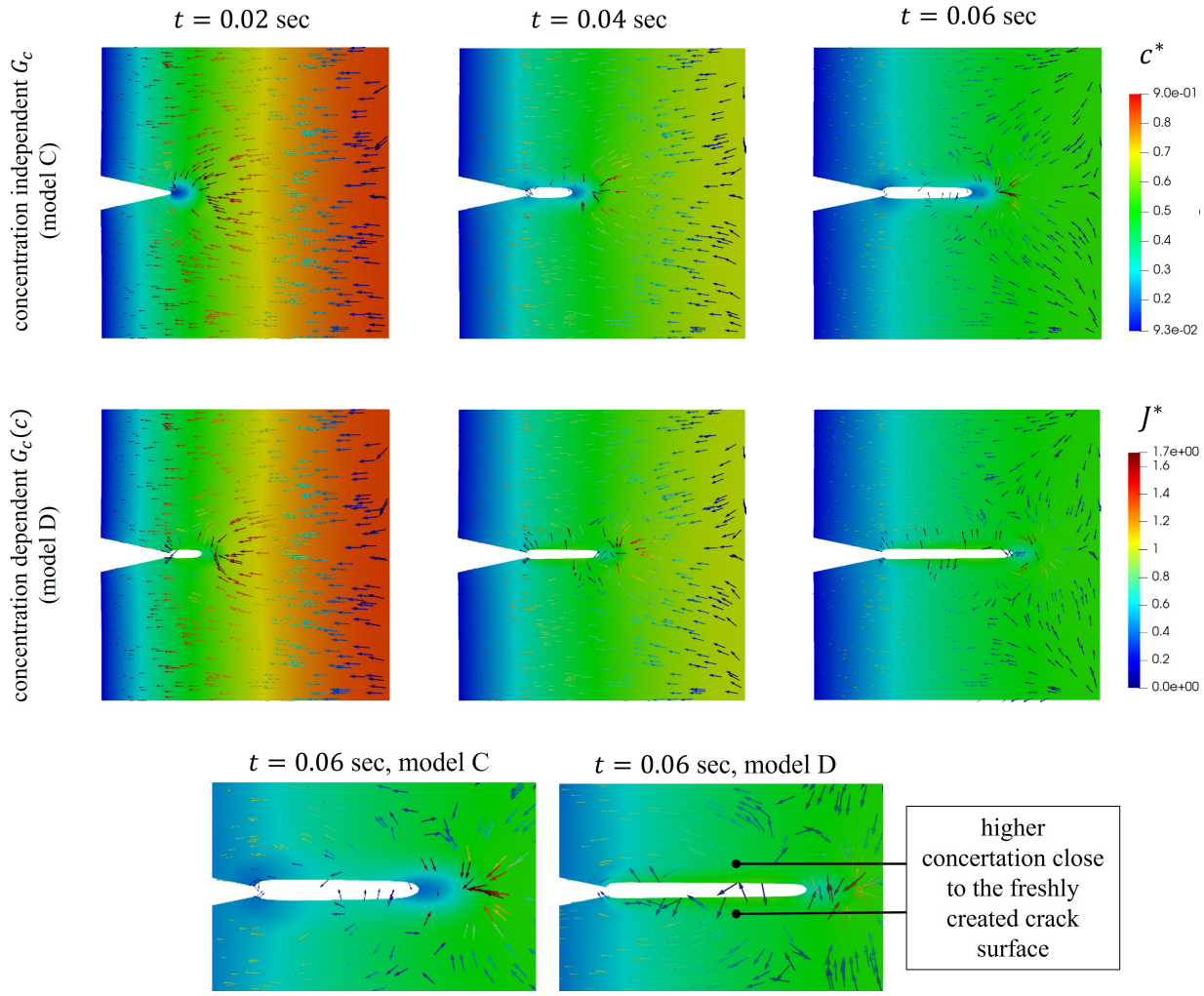

Figure 10: Comparison of results from formulations without and with concentration-dependent fracture toughness (model C and D) utilizing symmetric delithation BCs.

In Fig. 10, the simulation results for models C and D are compared. In model C, the fracture properties are assumed to be independent of the concentration (i.e. $G_c = G_{c,0}$). On the other hand, in model D, a linear drop is assumed for the fracture energy value $G_c(c) = G_{c,0}(1 - Wc/c_{max})$ where $W = 1$. As delithiation occurs, tensile stresses developed at the crack tip result in the accumulation of concentration. In model D, the additional concentration of Li-ions embrittles the material and therefore we observe earlier crack propagation initiation, i.e. smaller fracture resistance. Moreover, according to the third term in the right-hand side of Eq. 24 (i.e. $\gamma \dfrac{\mathrm{d}G_c(c)}{\mathrm{d}c}$), we expect additional flux term which drives the concentration to reach the crack surface. Such a tendency is energetically favorable for the system, as the free surface of the crack takes lower energy and with additional concentration. Concerning the latter point and since G_c reduces with concentration, the freshly created free surface is a suitable spot for species to navigate to. The reaction forces obtained from models C and D are compared in Fig. 11. As expected, by considering the effect of Li-embrittlement, we observe a significant drop in the calculated reaction force.

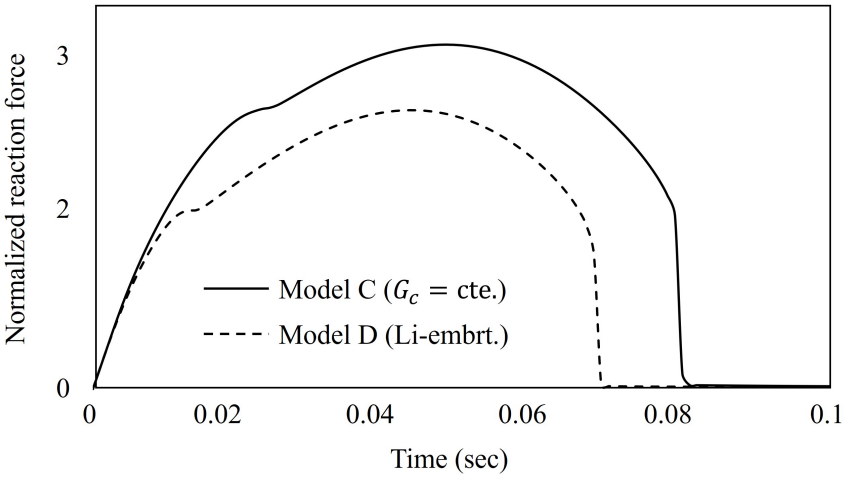

Figure 11: Comparison of obtained reaction forces from formulations without and with concentration-dependent fracture toughness (model C and D) utilizing symmetric delithation BCs.

4.5.1. Influence of preferential crack directions

Dependent on the microstructural features or nanoscopic structure of the material, there might exist some preferential direction for the crack. For example, one can mention the specific atomistic direction within the structure of a crystal. The latter is also known as the cleavage plane and can serve as a potential site for cracks to grow [95, 37].

By employing the anisotropy in the phase-field fracture model, we manage to include these features in the formulation (see also [47]). The same problem as before is considered for further studies. Instead, we introduce angle $\phi = 30°$ as the preferential crack direction. Furthermore, we set the parameter $\alpha = 10$ for this simulation (see Eq. 12 and explanations afterward). According to Fig. 12, upon symmetric delithation, the crack tends to deviate from the horizontal line. Such behavior is due to the high anisotropic properties we chose for the preferential crack direction (i.e. $\phi = 30°$). In other words, by applying the second-order tensor $\boldsymbol{A}$, we intentionally increase the fracture energy in any other direction compared to

the direction ϕ. As a result, the crack tends to go along the weakest direction which is shown in the first row of Fig. 12.

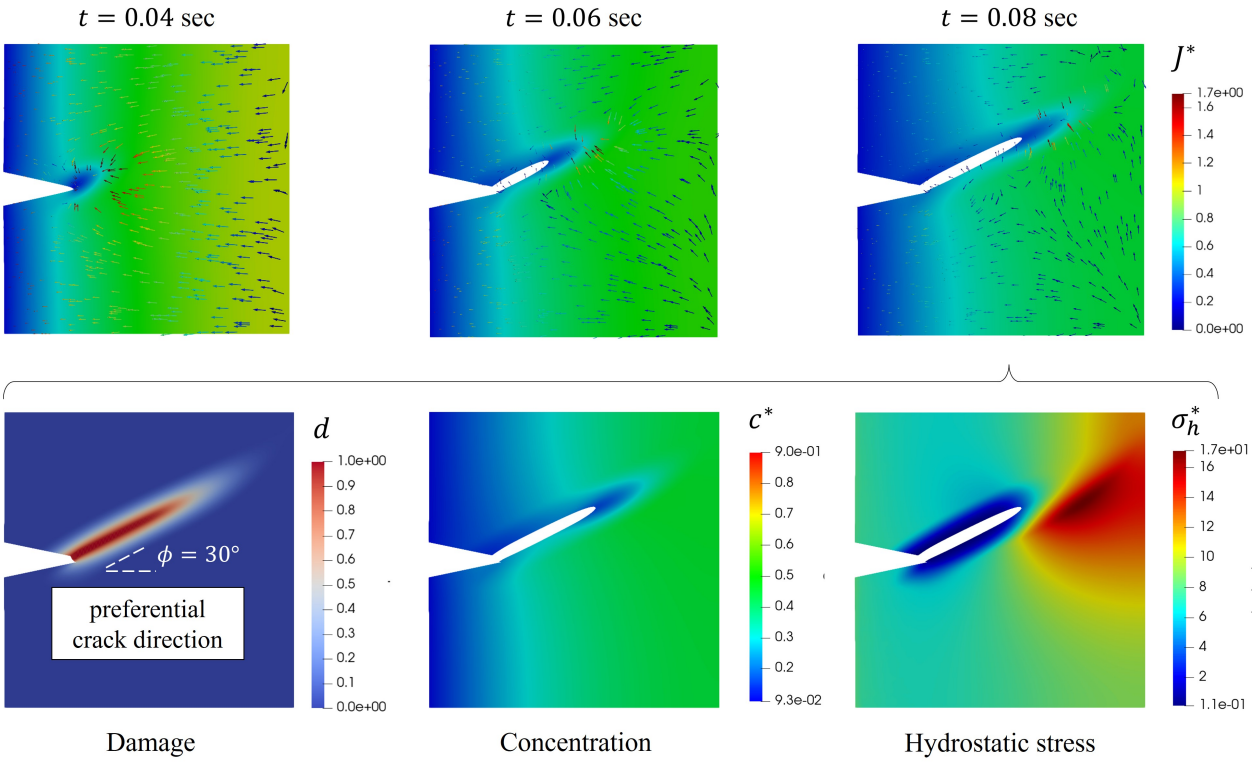

Figure 12: Comparison of concentration and flux profile for same concentration dependent fracture toughness and different slopes using Boundary condition A.

4.6. Chemomechanical fracture in single crystal active particle

In this part, one single crystal active material particle is investigated as shown in Fig. 13. Assuming the symmetric condition, one-quarter of the particle with a 2D-plane strain assumption is simulated. While 3D particles will be addressed in the later part of the article, this 2D assumption is still to a certain extent applicable for particular geometric cases e.g. long nanowires [94] as well as structural battery electrolyte [96].

A sufficiently fine mesh is chosen to ensure convergence. Details on the geometry and boundary conditions are summarized in Fig. 13. The material properties are according to Table 3. In particular, the fracture energy of the AM is assumed to be $G_{c0} = 0.25$ J/m^2. To regard roughly the crack nucleation due to surface defect, a pre-notch or pre-crack was introduced. For comparison, the case without pre-notch is also simulated, whereby the crack nucleation is difficult to interpret. A constant concentration of $c_{min} = 0.1\ c_{max}$ is defined on the outer region while the bulk concentration is defined as $c_0 = 0.9\ c_{max}$. The delithiation process is therefore achieved through the application of Dirichlet boundary conditions.

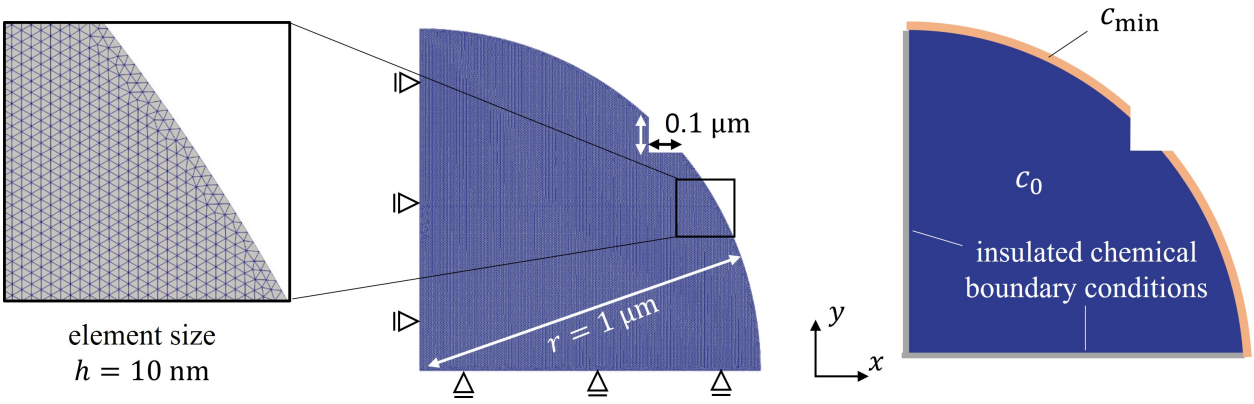

Figure 13: Geometry and boundary conditions of a circular active material.

In Fig. 14, the simulation results on the delithiation of the active material are shown. As we proceed from the left to the right, the delithiation process is getting completed. The presented results focus on how damage, normalized concentration, and hydrostatic stress profiles are evolving along the direction of the initial notch. Similar to the previous cases, the regions with damage higher than 0.8 are omitted for better visualization of the process and the internal length scale parameter is chosen as $l_c = 0.01$ μm. Based on the mechanical BCs, the outer surface of the active material goes under severe tensile stress as the concentration goes out of the system and the AM tends to shrink. This is similar to the previous test where the bulk tends to shrink but it is under mechanical constraints. High tension at the outer circumference of the circle serves as an ideal spot for crack nucleation and propagation.

In Fig. 15, we repeat the same delithiation process where we do not have any pre-crack in the system. Therefore, the location of the crack nucleation is now more or less arbitrary, since they are mostly induced by numerical fluctuation. Here, we observed two main cracks evolving simultaneously. The location of these cracks may change if we slightly change the simulation parameters (e.g. delithiation rate or some convergence criterion). However, the distance between the cracks (number of major evolving cracks in total) stays the same for the given material system. This observation is according to similar tests related to periodic cracking in the materials [97] or quench test [98]. Furthermore, here the depth of the cracks at the final time is slightly lower than the crack length in Fig. 14. Therefore, the number of cracks and their propagation depth seem to be strongly related to the available elastic energy.

Next, we investigate an example where the delithiation process is performed for the case where we take into account phase transformation (PT) within the active material solid. In order to achieve phase transition in the material $\chi = 2.4$ and for a sharp interface between the phases $\kappa = 1.2 \times 10^{-12}$ Jm^{2}mol^{-1} is used [55]. In Fig. 16 the results for the notched case are presented. Although at the initial crack tip, the stresses are building up, cracks in the system tend to initiate from the outer surface where we observe much higher stresses which are now enhanced due to PT. The reason for this higher stress is the formation of high and low concentration regions during the phase transformation, which creates a huge change from the stress-free concentration at the outer surface of the particle, and therefore higher tensile stress is observed in that area which leads to crack nucleation. Interestingly,

the number and depth of cracks at the end are enough to dissipate the energy and therefore we did not observe crack propagation from the notch. Here one should note that the depth of the initial notch does play a role and upon selecting other sizes cracking may start from the notch as well. In Fig. 17 we omit the initial notch and studied the crack evolution. Similar to the case without PT, we ended up with more or less equidistant cracking in the system. The main conclusion at this point is the major influence of the PT zone which controls not only the crack initiation but also the evolution of the crack front (see also studies in [99]).

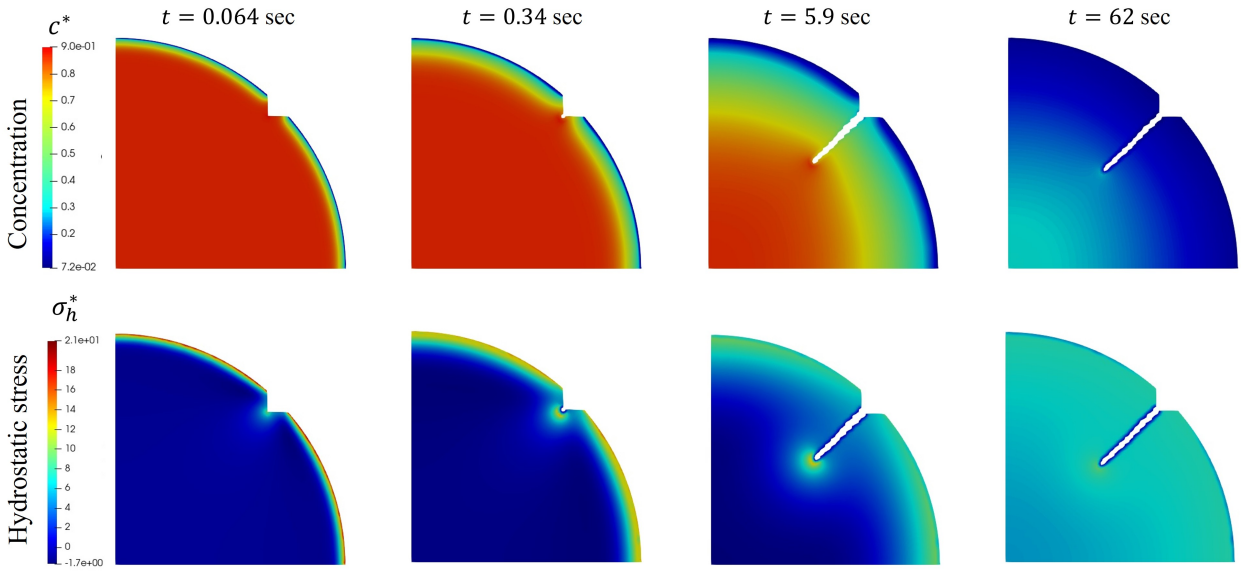

Figure 14: Evolution of damage, concentration, and stress profile in the active material with the initial notch. There is no phase transition in the solid AM as the concentration changes.

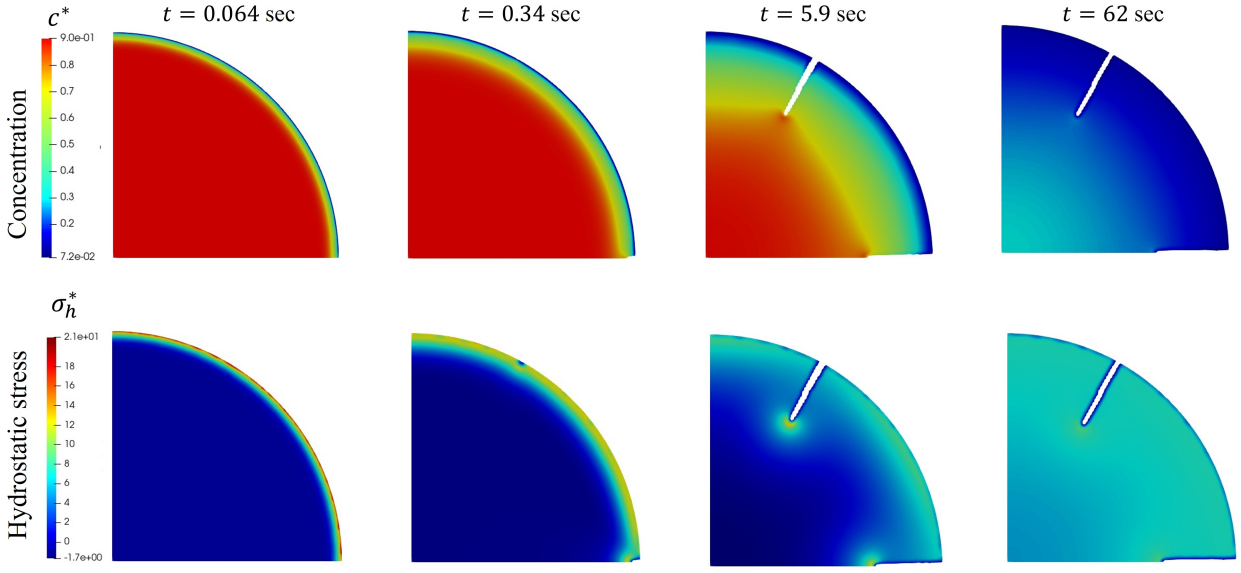

Figure 15: Evolution of damage, concentration, and stress profile in the active material without any initial notch. There is no phase transition in the solid AM as the concentration changes.

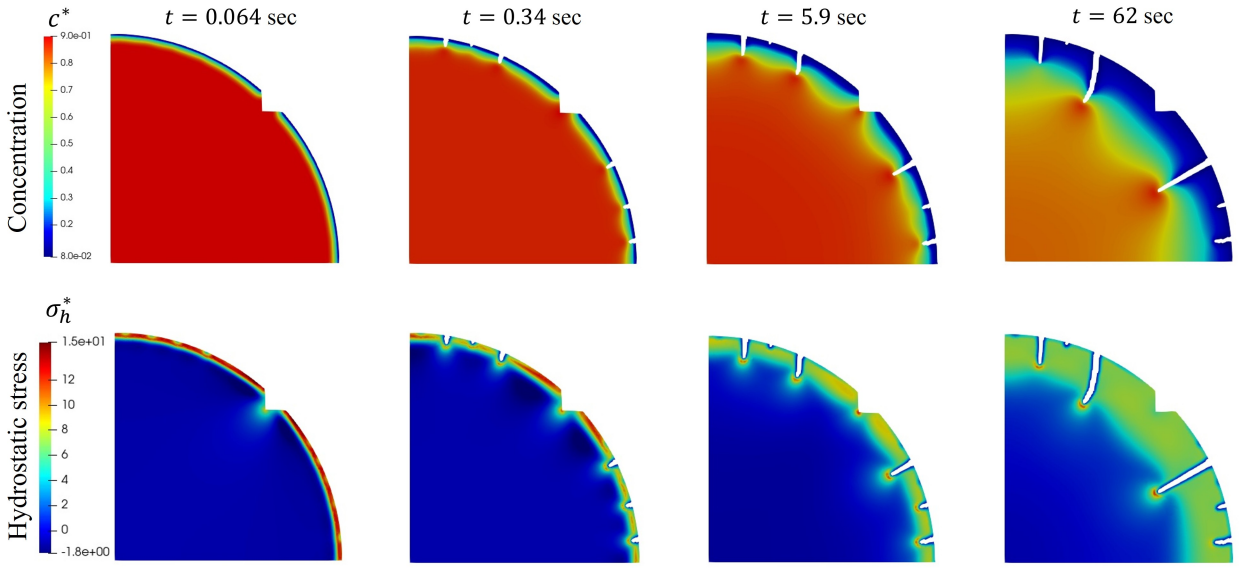

Figure 16: Evolution of damage, concentration, and stress profile in the active material with the initial notch. The solid AM goes under phase transformation as the concentration changes.

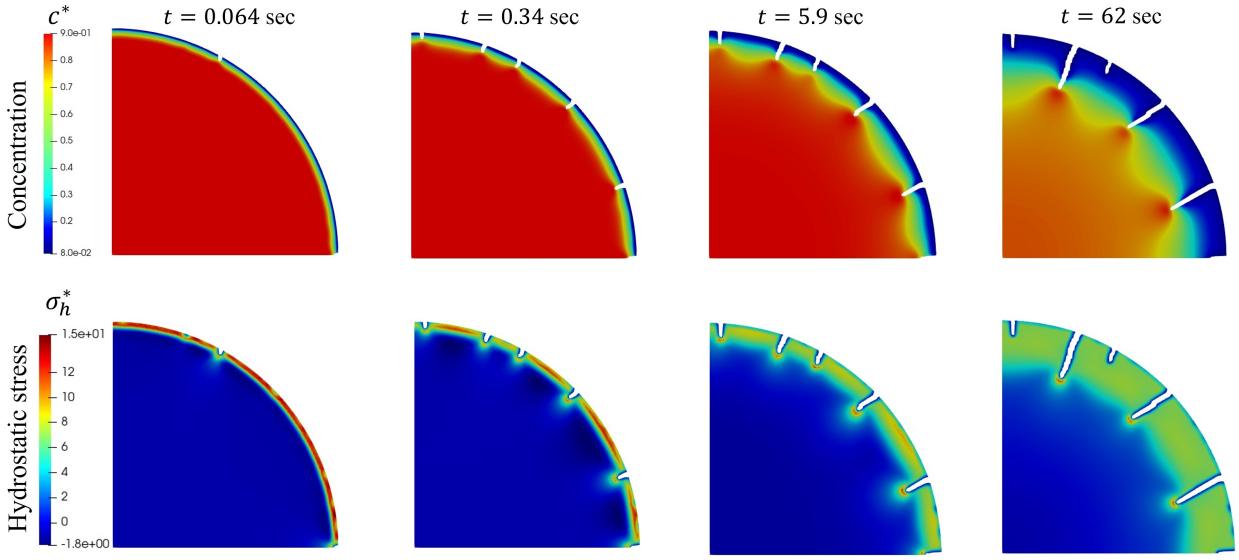

Figure 17: Evolution of damage, concentration, and stress profile in the active material without any initial notch. The solid AM goes under phase transformation as the concentration changes.

Despite insightful studies in a 2D setting, in many realistic cases, we are dealing with 3D particles where we cannot apply the 2D assumptions. While the theoretical formulation and numerical implementation remain the same or similar for 2D or 3D cases, the computation cost and the particular simulation results vary. In Fig. 18, the geometry, finite element meshing as well as mechanical and chemical boundary conditions for a spherical AM particle are shown from left to right, respectively. Again, we take advantage of certain symmetric planes and reduce the model to 1/8 of the original one. The particle goes under delithiation. Note that a pre-crack is also introduced in the shape of an ellipse to facilitate cracking.

The results of this process in terms of the damage and concentration profile are reported in Fig. 19. Interestingly, due to the 3D nature of the problem, the cracks not only propagate the y-z plane towards the center of the particle but also another crack start to propagate from the surface toward the depth of the particle as shown at time $t = 2.6$ sec. Again, we observe a similar pattern here where the cracks seem to get maximum distance from each other.

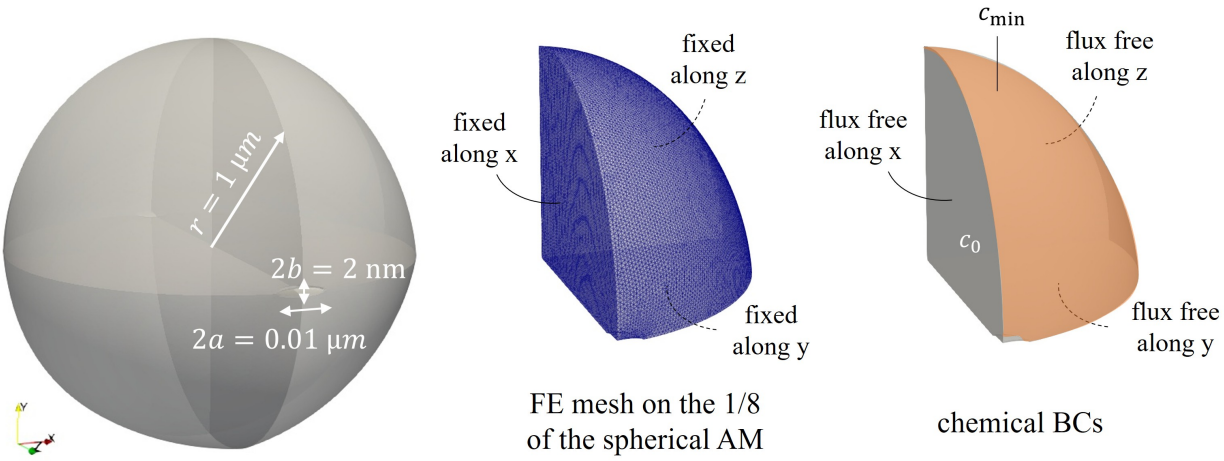

Figure 18: Geometry and boundary conditions of a spherical active material.

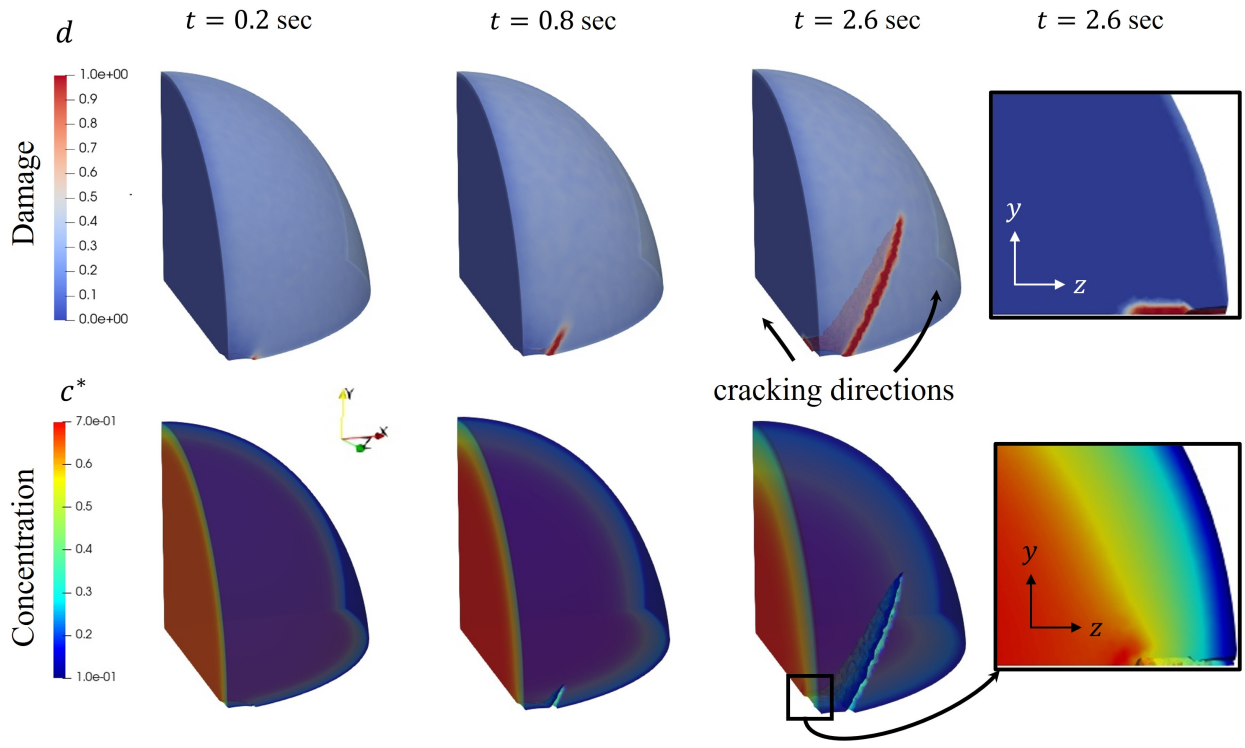

Figure 19: Evolution of damage and concentration profile in the 3D active material with a penny-shaped initial notch. There is no phase transition in the solid AM as the concentration changes.

4.7. Cracking in a heterogeneous chemo-mechanically coupled environment

To make the advantage of the current modeling approach clear, a simulation is performed for two neighboring grains in a polycrystalline active material. In Fig. 20, the grain boundary region is replaced by a thin layer where the thickness of the GB is set to 20 nm. the system is delithiated from the left-hand side and we have studied two different values for the fracture energy of the GB region. Other BCs as well as geometrical information are reported in 20 and the material properties are based on Table 3. The results reported in Fig. 21 clearly show that in the case of a very weak GB (i.e. where the fracture and elastic properties are reduced by a factor of 10), the transgranular crack pattern will change into the intergranular mode. Note that the same formulation is utilized for all the FE meshes but simply the properties assigned to the model are varied to represent the heterogeneity within the system. Here the question remains of how to properly distribute the material properties which shall be the point for future investigations. See also studies in [100, 64].

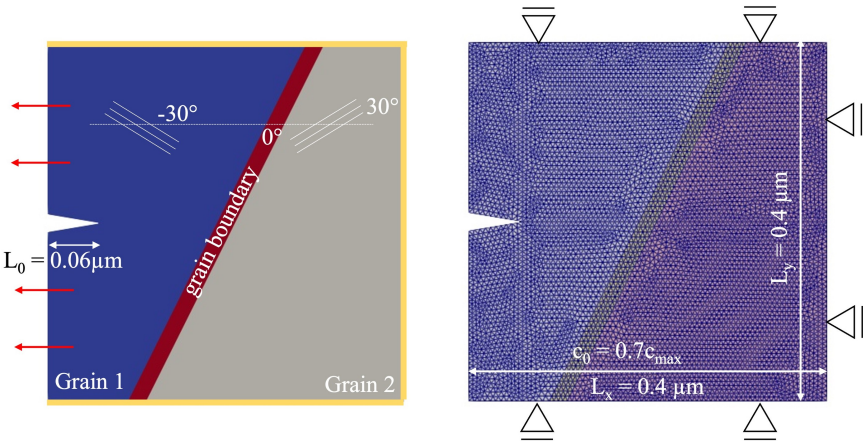

Figure 20: Average damage evolution during the simulation of the current model.

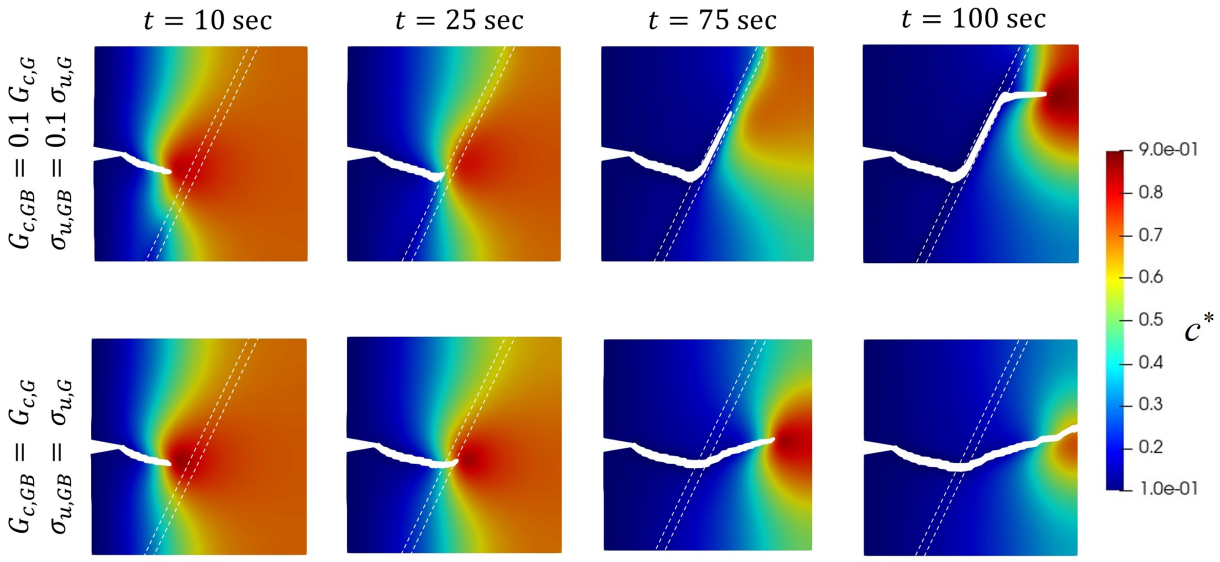

Figure 21: Average damage evolution during the simulation of the current model.

4.8. Initial studies on damage progression in composite cathodes in solid-state batteries

Next, we focus on the previous example by adding the solid electrolyte phase around the active particle according to Fig. 22. The interface between the SE and the AM is enriched with a new set of chemo-mechanical coupled CZ elements where the flux vector is in accordance with Eq. 28. In the current work, this interface is represented by a CZ model described in [3]. Such a model can also be represented by an electro-chemo-mechanical cohesive PF model in future development and it is not the focus of the current study. The delithiation process is modeled in this study. The AM is modeled by means of the described chemo-mechanical coupled PF fracture model while the SE part is modeled via model A (uncoupled chemo-mechanical model) without any damage. To trigger the crack initiation for this numerical study, the value for fracture energy of the AM is changed to $G_{c0} = 0.03$ J/m^2 and $\sigma_{u0} = 60$ MPa. Furthermore, the governing equation for the c_e inside the electrolyte is the simple Fickian diffusion: $\dot{c_e} = \nabla \cdot (D_e \nabla c_e)$. Here we assumed that the change in the electrolyte's concentration is small during the chemical diffusion and as a result, no change in the electrolyte's volume is expected in response to the concentration change. Moreover and due to simplicity, the electric potential is not considered for this study. As a result, the migration of the Li ions due to the electric field is not considered in the electrolyte. The parameters for the SE are summarized in Table 5. The parameters for the AM are the same as before.

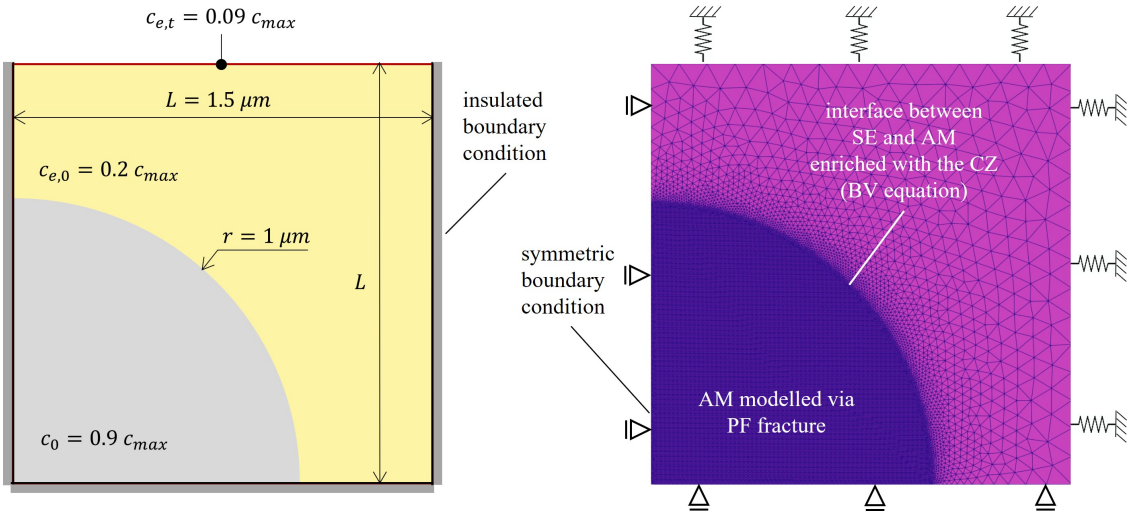

Figure 22: Simulation setup for the delithiation process in a composite cathode including an active material surrounded by a solid electrolyte.

A constant concentration $c_{e,t} = 0.09\ c_{max}$ is applied on the upper edge. Based on the given BCs, delithation happens inside the SE. Moreover, based on the introduced electrochemical reaction at the interface between the AM and SE (BV relation), an outward flux of species occurs which in return results in delithiation of the AM. Due to the shrinkage of the AM as well as mechanical constraints on its surroundings crack patterns will start to form according to Fig. 23. Interestingly enough, the cracks seem to start in a radial fashion similar to the case of liquid electrolytes, but after a while and based on the new stress distributions, cracks tend to propagate in a circumferential direction. In other words, adding the solid electrolyte

tends to change the dominant fracture mode which was also observed in similar studies by the authors in polycrystalline AM [3]. The obtained results for the concentration profile as well as chemical flux are reported in Fig. 24.

	Unit	Value
Young's modulus of electrolyte E	[GPa]	43
Poisson's ratio of electrolyte ν	[-]	0.2
Diffusivity of electrolyte D_e	[m^2/s]	5.4×10^{-15}
Surface site concentration c_{surf}	[mol/m^2]	6.78×10^{-6}
Single reaction step time τ_0	[s]	0.01
Voltage drop $\Delta\phi$	[mV]	4.88

Table 5: Parameters used for the electrolyte in the numerical examples taken from [55, 101].

As expected, based on the cracking mechanics, a major part of the AM is now disconnected from the process which results in a performance drop for the battery at larger scales. We should emphasize that based on our early studies, the interface's mechanical properties play a role here as well. Such studies as well as investigations on different shapes of AM and elastic properties of the SE material should be a subject for future studies. The latter investigation can lead to a huge improvement in the design of a new generation of batteries.

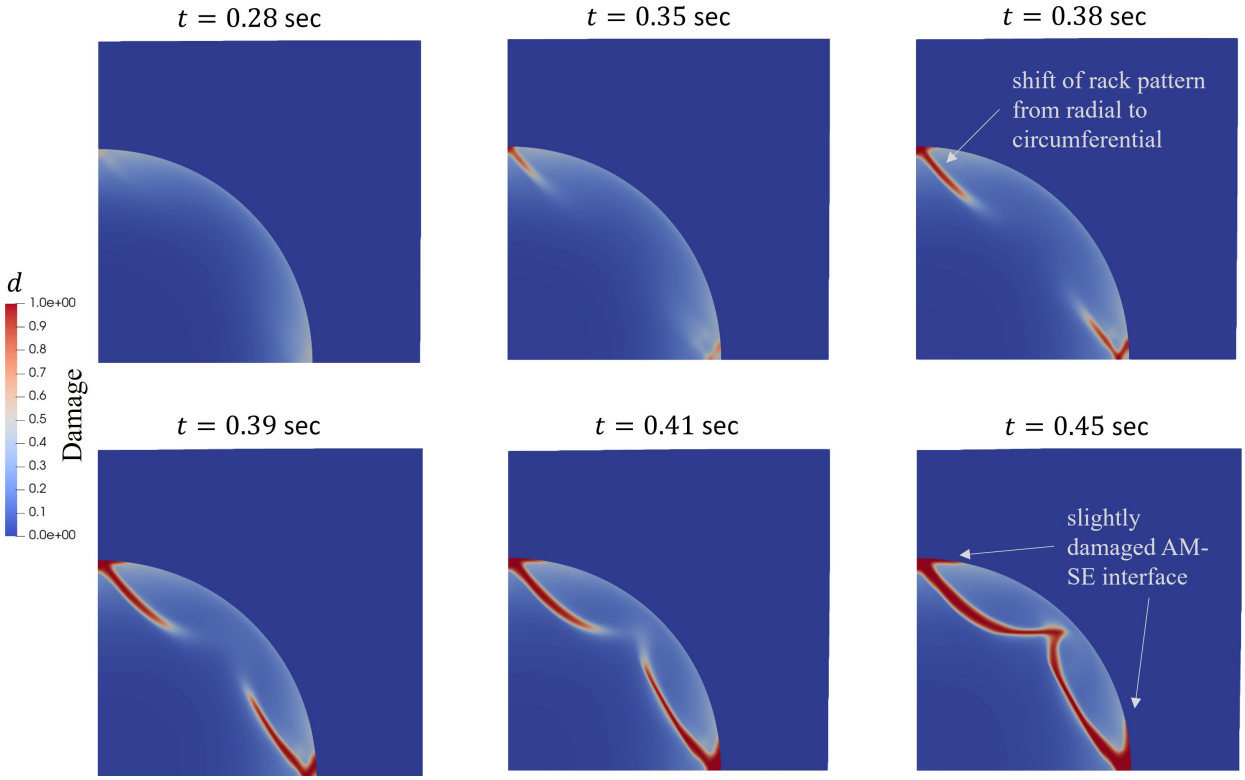

Figure 23: Fracture mode changes when the solid electrolyte comes into the picture.

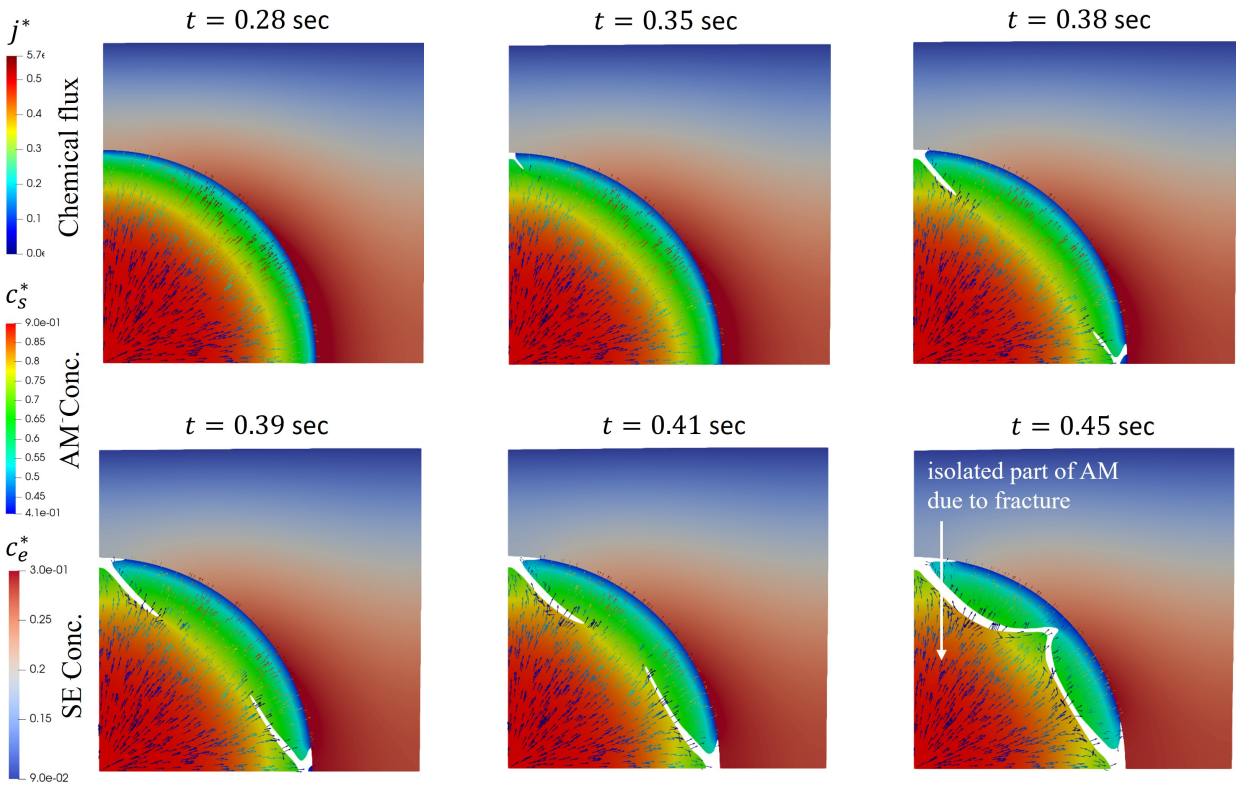

Figure 24: Results of concentration profile for a composite cathode system in a solid-state battery. Due to fracture, material points inside the AM are disconnected and out of usage for the next cycle of lithiation.

5. Conclusion and future work

In this contribution, a chemo-mechanical coupled phase-field fracture model is developed which takes into account the cohesive nature of the fracture. The developed model can depict fracture without a predefined trajectory for the crack path. The model is derived based on a consistent formulation and respects the thermodynamical aspects in a chemo-mechanical coupled environment. The implementation of the model in a finite element program is described in detail. Moreover, through various numerical studies, the efficiency of the model and its ability to accurately predict fracture in a chemical environment are examined. The model highlights the coupling terms between mechanics, damage, and diffusion. The formulation is then used to perform studies on solid-state battery systems. Nevertheless, the framework is generally discussed, making it available for other similar applications where we have the interaction of mechanics and diffusion.

Another contribution of this work is a detailed study of the influence of different coupling terms on the predicted results. We concluded that the impact of hydrostatic stress can severely change the concentration and flux distribution which in return changes the crack initiation/propagation behavior. The same holds for including the influence of the damage field in the chemical part. By degradation of the flux vector, one can obtain a physically reasonable distribution for the concentration profile. Finally, upon choosing concentration-dependent fracture properties, one can predict the damage progression considering Li-embrittlement. Phase transformation within the solid upon changing of concentration produces high stresses

in the transition zone. The latter point facilitates cracking compare to the case where we do not have phase transition. For the specific application at hand, we concluded that the obtained crack pattern severely changes by replacing the liquid electrolyte with a solid one. For the case of a liquid electrolyte and a circular AM, the crack patterns are in a radial direction which is also confirmed by the previous studies in the literature. On the other hand, by considering the effect of the SE, the crack patterns tend to change in the circumferential direction keeping other conditions the same. The latter point results in the disconnection of the inner part of the AM from the rest of the system and therefore one expects a considerable capacity loss in the next cycles.

In the future contribution, one should focus on further numerical studies where cyclic lithiation and delithiation are under focus for 2D as well as 3D particles. In this work, a constant Irwin's length was assumed. In other words, it would be interesting to examine what will happen if the degradation function is also concentration-dependent. The latter point specifically becomes important when we have access to concentration-dependent fracture properties from the lower scale. See for example [102, 37] for calibration of damage continuum models with atomistic data. The influence of phase transition with respect to Li concentration should be further studied as it severely affects the cracking mechanism in the solid. The chemical interphases influence the crack initiation behavior and the way it propagates [55, 103, 104, 94]. The introduced model can also be applied in examples including polycrystalline materials by introducing additional indicating parameters to show the smooth transition between different phases (grains) [100]. Finally, it is rewarding to apply the model for optimization of the AM particle geometry or material properties to increase the performance of the batteries and use this knowledge for simulations at the cell level [77, 105].

Acknowledgements:
The authors gratefully acknowledge the computing time granted on the Hessian High-Performance Computer "Lichtenberg". This work has been partially funded by the German Research Foundation DFG under grant STE 2350/1-1.

Disclaimer:
The results, opinions, and conclusions expressed in this publication are not necessarily those of Volkswagen Aktiengesellschaft.

Author Statement:
Shahed Rezaei: Conceptualization, Methodology, Supervision, Writing - Review & Editing. Jacob Niikoi Okoe-Amon: Methodology, Software, Writing - Review & Editing. Cerun Alex Varkey: Methodology, Software, Writing - Review & Editing. Armin Asheri: Software, Methodology, Review & Editing. Hui Ruan: Software, Methodology, Review & Editing. Bai-Xiang Xu: Methodology, Supervision, Funding acquisition, Review & Editing.

6. Appendix A: First and second laws of thermodynamic

Considering kinetic energy rate as well as internal and external power equations, the energy balance equation is simplified as:

$$\int_V \rho\ \dot{e}\ dV = \int_V \boldsymbol{\sigma} : \dot{\boldsymbol{\varepsilon}}\ dV \tag{40}$$

$$+ \int_V \mu \dot{c}\ dV + \int_V \boldsymbol{\zeta} \cdot \boldsymbol{n} \dot{c}\ dV - \int_V \boldsymbol{J} \cdot (\nabla \mu)\ dV \tag{41}$$

$$- \int_V \nabla \cdot \boldsymbol{q}\ dV + \int_V \rho\ r\ dV - \int_V Y \dot{d}\ dV - \int_V \boldsymbol{H} \cdot \nabla \dot{d}\ dV. \tag{42}$$

In the above equations, ρ is the material density, and $\dot{e}$ is the solid's internal energy per volume. Derivation with respect to time is denoted by $\dot{(\ )}$. The stress and strain tensors are denoted by $\boldsymbol{\sigma}$ and $\boldsymbol{\varepsilon}$, respectively. The quantity μ is the chemical potential, $\boldsymbol{J}$ is the chemical flux, and $\boldsymbol{\zeta}$ is the so-called micro-stress vector. Moreover, r is the heat source, and $\boldsymbol{q}$ is the heat flux. Finally, Y and $\boldsymbol{H}$ are the damage driving force and the internal micro-traction, respectively. The local form of the above relation reads:

$$\rho\ \dot{e} - \boldsymbol{\sigma} : \dot{\boldsymbol{\varepsilon}} - \mu \dot{c} + (\nabla \cdot \boldsymbol{\zeta})\, \dot{c} + \boldsymbol{\zeta} \cdot \nabla \dot{c} + \boldsymbol{J} \cdot (\nabla \mu) + \nabla \cdot \boldsymbol{q} - \rho\ r\ + Y \dot{d} + \boldsymbol{H} \cdot \nabla \dot{d} = 0. \tag{43}$$

Defining entropy rate as $\dot{S}$, and temperature as T, the second law of thermodynamic reads

$$\dot{S} \geq - \int_{\partial V} \frac{\boldsymbol{n} \cdot \boldsymbol{q}}{T}\ dS + \int_V \rho \frac{r}{T}\ dV. \tag{44}$$

By applying Gauss' Theorem, one can further write the above relation as

$$\dot{S} \geq - \int_V \frac{1}{T} \nabla \cdot \boldsymbol{q}\ dV + \int_V \frac{1}{T^2}\ \boldsymbol{q} \cdot \nabla T\ dV + \int_V \frac{1}{T}\ \rho\ r\ dV. \tag{45}$$

The entropy rate is then obtained based on the specific entropy rate $\dot{s}$ according to $\dot{S} = \int_V \rho \dot{s}\ dV$. As a result, the local form of Eq. 45 is written as follows where both sides of the equation are multiplied by the absolute temperature value:

$$\rho T \dot{s} + \nabla \cdot \boldsymbol{q} - \frac{1}{T}\ \boldsymbol{q} \cdot \nabla T - \rho r \geq 0 \tag{46}$$

By substituting $\nabla \boldsymbol{q}$ from the 1st law (Eq. 43) into the 2nd law (Eq. 46), we obtain

$$\rho T \dot{s} - \rho \dot{e} + \boldsymbol{\sigma} : \dot{\boldsymbol{\varepsilon}} + \mu \dot{c} + (\nabla \cdot \boldsymbol{\zeta})\, \dot{c} + \boldsymbol{\zeta} \cdot \nabla \dot{c} - \boldsymbol{J} \cdot (\nabla \mu) - \frac{\boldsymbol{q}}{T} \cdot \nabla T + Y \dot{d} + \boldsymbol{H} \cdot \nabla \dot{d} \geq 0. \tag{47}$$

The rate of internal energy is further defined as

$$\dot{e} = \dot{\psi} + \dot{T} s + T \dot{s} \tag{48}$$

As a result, the Clausius-Duhem inequality is written as

$$\boldsymbol{\sigma} : \dot{\boldsymbol{\varepsilon}} - \rho \dot{\psi} + \mu \dot{c} + (\nabla \cdot \boldsymbol{\zeta})\, \dot{c} + \boldsymbol{\zeta} \cdot \nabla \dot{c} - \boldsymbol{J} \cdot \nabla \mu + Y \dot{d} + \boldsymbol{H} \cdot \nabla \dot{d} - \rho\ \dot{T} s - \frac{\boldsymbol{q}}{T} \cdot \nabla T \geq 0. \tag{49}$$

Based on the isothermal and adiabatic assumptions in the system, the last two terms in Eq. 49 will vanish and we end up with the relation in Eq. 4.

7. Appendix B: Implementation aspects in the MOOSE framework

Further details and explanations regarding the code's implementation are given below to help readers understand the different steps from coding to scripting an input file. Considering the MOOSE framework, a graphical representation is provided in Fig. 25. One should note the following description is not necessarily a fixed order that must be followed chronologically, although it is recommended.

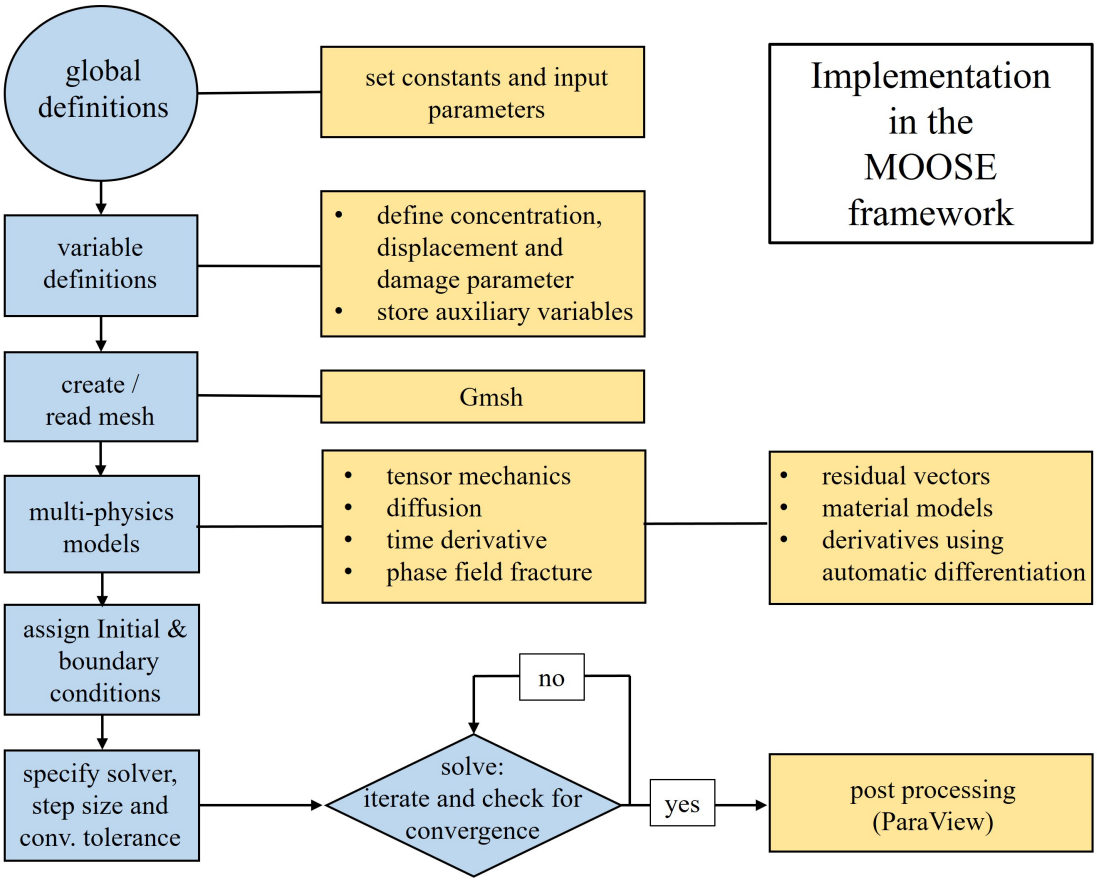

Figure 25: MOOSE implementation of the chemo-mechanical cohesive phase-field model.

The input file is scripted according to Fig. 25. Global parameters including elastic properties, fracture toughness, and the ultimate stress among others are first defined. Next, a mesh was created utilizing the software package Gmsh. Then different variables are declared and initial values are defined when necessary. For the main input file (which represents the master app), displacement variables in x and y directions as well as concentration value are defined (i.e. $\boldsymbol{u}$ and c). Also, auxiliary variables are defined to store values of interest to be used during the FE analysis.

The next step is to specify the multiphysics models by calling onto the codes written within the files in the Kernel block of the input file. Each kernel (coded residual) is assigned as a 'type' with an already defined variable assigned to be solved for. In summary, a kernel called upon to solve divergence of stress will for instance have the variables for displacement

in x and y directions assigned to it. The coupled diffusion code is also called upon and the concentration variable is given to be worked on.

To solve residuals in the kernel block, certain material models are needed to calculate material properties and functions. For instance, a material model is needed to solve for a varying chemical eigen-strain to account for the change in strain throughout the material. In this study, Automatic Differentiation (AD) is called upon to help solve the Jacobian and provide derivatives as needed for the simulation.

Boundary conditions that apply to the variables and the geometry being simulated are then defined. After which, the executioner is defined. The executioner includes the solve type, the time step, the end time, the relative tolerance, and the absolute tolerance. Relative tolerance of 1×10^{-8} is defined to determine the convergence of each iterative step before moving on to the next iteration. A time stepper block is defined within the executioner lock to address issues of non-convergence and factors by which the time step should be cut back or increased.

An initial time step of 2×10^{-7} is defined in the input file. This time step is not necessarily what the simulation is completed with. As mentioned, it can be increased or cut back depending on the convergence of the simulation. For the case of the multi-app as described above in Fig. 3, an additional block is included in the input file, where transfers are made from and to the main/master app and the sub-app. The sub-app includes damage input file which follows the above-described procedure. This sub-app focuses mainly on solving the damage residual and its associated material models (see governing equations for damage described throughout this work). More explanations and codes are available for interested users upon request.

References

[1] F. Zhang, Q.-A. Huang, Z. Tang, A. Li, Q. Shao, L. Zhang, X. Li, J. Zhang, A review of mechanics-related material damages in all-solid-state batteries: Mechanisms, performance impacts and mitigation strategies, Nano Energy 70 (2020) 104545.

[2] D. A. Santos, S. Rezaei, D. Zhang, Y. Luo, B. Lin, A. R. Balakrishna, B.-X. Xu, S. Banerjee, Chemistry–mechanics–geometry coupling in positive electrode materials: a scale-bridging perspective for mitigating degradation in lithium-ion batteries through materials design, Chem. Sci. (2023).

[3] S. Rezaei, A. Asheri, B.-X. Xu, A consistent framework for chemo-mechanical cohesive fracture and its application in solid-state batteries, Journal of the Mechanics and Physics of Solids 157 (2021) 104612.

[4] J. Janek, W. G. Zeier, A solid future for battery development, Nature Energy 1 (2016).

[5] M. Pasta, D. Armstrong, Z. L. Brown, J. Bu, M. R. Castell, P. Chen, A. Cocks, S. A. Corr, E. J. Cussen, E. Darnbrough, V. Deshpande, C. Doerrer, M. S. Dyer, H. El-Shinawi, N. Fleck, P. Grant, G. L. Gregory, C. Grovenor, L. J. Hardwick, J. T. S. Irvine, H. J. Lee, G. Li, E. Liberti, I. McClelland, C. Monroe, P. D. Nellist, P. R.

Shearing, E. Shoko, W. Song, D. S. Jolly, C. I. Thomas, S. J. Turrell, M. Vestli, C. K. Williams, Y. Zhou, P. G. Bruce, 2020 roadmap on solid-state batteries, Journal of Physics: Energy 2 (2020) 032008.

[6] X. Liu, B. Zheng, J. Zhao, W. Zhao, Z. Liang, Y. Su, C. Xie, K. Zhou, Y. Xiang, J. Zhu, H. Wang, G. Zhong, Z. Gong, J. Huang, Y. Yang, Electrochemo-mechanical effects on structural integrity of ni-rich cathodes with different microstructures in all solid-state batteries, Advanced Energy Materials 11 (8) (2021) 2003583.

[7] L. Cheng, W. Chen, M. Kunz, K. Persson, N. Tamura, G. Chen, M. Doeff, Effect of surface microstructure on electrochemical performance of garnet solid electrolytes, ACS Appl. Mater. Interfaces 7 (3) (2015) 2073–2081.

[8] J. A. Lewis, J. Tippens, F. J. Q. Cortes, M. T. McDowell, Chemo-mechanical challenges in solid-state batteries, Trends in Chemistry (2019).

[9] W. S. LePage, Y. Chen, E. Kazyak, K.-H. Chen, A. J. Sanchez, A. Poli, E. M. Arruda, M. D. Thouless, N. P. Dasgupta, Lithium mechanics: Roles of strain rate and temperature and implications for lithium metal batteries, Journal of The Electrochemical Society 166 (2) (2019) A89–A97.

[10] S. Hao, J. J. Bailey, F. Iacoviello, J. Bu, P. S. Grant, D. J. L. Brett, P. R. Shearing, 3d imaging of lithium protrusions in solid-state lithium batteries using x-ray computed tomography, Advanced Functional Materials 31 (10) (2021) 2007564.

[11] D. Cao, X. Sun, Q. Li, A. Natan, P. Xiang, H. Zhu, Lithium dendrite in all-solid-state batteries: Growth mechanisms, suppression strategies, and characterizations, Matter (2020).

[12] C. Yuan, X. Gao, Y. Jia, W. Zhang, Q. Wu, J. Xu, Coupled crack propagation and dendrite growth in solid electrolyte of all-solid-state battery, Nano Energy 86 (2021) 106057.

[13] S. S. Shishvan, N. A. Fleck, V. S. Deshpande, The initiation of void growth during stripping of li electrodes in solid electrolyte cells, Journal of Power Sources 488 (2021) 229437.

[14] B. S. Vishnugopi, M. B. Dixit, F. Hao, B. Shyam, J. B. Cook, K. B. Hatzell, P. P. Mukherjee, Mesoscale interrogation reveals mechanistic origins of lithium filaments along grain boundaries in inorganic solid electrolytes, Advanced Energy Materials 12 (3) (2022) 2102825.

[15] L. Porz, T. Swamy, B. W. Sheldon, D. Rettenwander, T. Frömling, H. L. Thaman, S. Berendts, R. Uecker, W. C. Carter, Y.-M. Chiang, Mechanism of lithium metal penetration through inorganic solid electrolytes, Advanced Energy Materials 7 (20) (2017) 1701003.

[16] R. Xu, K. Zhao, Corrosive fracture of electrodes in li-ion batteries, Journal of the Mechanics and Physics of Solids 121 (2018) 258 – 280.

[17] K. Min, C. Jung, D.-S. Ko, K. Kim, J. Jang, K. Park, E. Cho, High-performance and industrially feasible ni-rich layered cathode materials by integrating coherent interphase, ACS Applied Materials & Interfaces 10 (24) (2018) 20599–20610.

[18] H.-H. Ryu, K.-J. Park, C. S. Yoon, Y.-K. Sun, Capacity fading of ni-rich cathodes for high-energy-density lithium-ion batteries: Bulk or surface degradation?, Chem. Mater. 30 (3) (2018) 1155–1163.

[19] H. Liu, M. Wolf, K. Karki, Y.-S. Yu, E. A. Stach, J. Cabana, K. W. Chapman, P. J. Chupas, Intergranular cracking as a major cause of long-term capacity fading of layered cathodes, Nano Letters 17 (6) (2017) 3452–3457.

[20] G. Sun, T. Sui, B. Song, H. Zheng, L. Lu, A. M. Korsunsky, On the fragmentation of active material secondary particles in lithium ion battery cathodes induced by charge cycling, Extreme Mechanics Letters 9 (2016) 449 – 458, mechanics of Energy Materials.

[21] H. Kim, M. G. Kim, H. Y. Jeong, H. Nam, J. Cho, A new coating method for alleviating surface degradation of lini0.6co0.2mn0.2o2 cathode material: Nanoscale surface treatment of primary particles, Nano Letters 15 (3) (2015) 2111–2119.

[22] D. Bistri, C. V. D. Leo, Modeling of chemo-mechanical multi-particle interactions in composite electrodes for liquid and solid-state li-ion batteries, Journal of The Electrochemical Society 168 (3) (2021) 030515.

[23] R. Xu, Y. Yang, F. Yin, P. Liu, P. Cloetens, Y. Liu, F. Lin, K. Zhao, Heterogeneous damage in li-ion batteries: Experimental analysis and theoretical modeling, J. Mech. Phys. Solids 129 (2019) 160 – 183.

[24] R. Koerver, I. Aygün, T. Leichtweiß, C. Dietrich, W. Zhang, J. O. Binder, P. Hartmann, W. G. Zeier, J. Janek, Capacity fade in solid-state batteries: Interphase formation and chemomechanical processes in nickel-rich layered oxide cathodes and lithium thiophosphate solid electrolytes, Chem. Mater. 29 (13) (2017) 5574–5582.

[25] J. Ma, B. Chen, L. Wang, G. Cui, Progress and prospect on failure mechanisms of solid-state lithium batteries, J. Power Sources 392 (2018) 94 – 115.

[26] B. Sun, W. Lu, B. Gault, R. Ding, S. K. Makineni, D. Wan, C.-H. Wu, H. Chen, D. Ponge, D. Raabe, Chemical heterogeneity enhances hydrogen resistance in high-strength steels, Nature Materials (2021).

[27] A. Wang, S. Kadam, H. Li, S. Shi, Y. Qi, Review on modeling of the anode solid electrolyte interphase (sei) for lithium-ion batteries, npj Computational Materials 4 (2018).

[28] P. Wang, W. Qu, W.-L. Song, H. Chen, R. Chen, D. Fang, Electro–chemo–mechanical issues at the interfaces in solid-state lithium metal batteries, Advanced Functional Materials 29 (27) (2019) 1900950.

[29] K. Zhao, Mechanics in li-ion batteries, in: Reference Module in Earth Systems and Environmental Sciences, Elsevier, 2021.

[30] Y. Zhao, P. Stein, Y. Bai, M. Al-Siraj, Y. Yang, B.-X. Xu, A review on modeling of electro-chemo-mechanics in lithium-ion batteries, Journal of Power Sources 413 (2019) 259 – 283.

[31] D. Bistri, A. Afshar, C. V. Di Leo, Modeling the chemo-mechanical behavior of all-solid-state batteries: a review, Meccanica (2020) 1572–9648.

[32] E. J. Cheng, A. Sharafi, J. Sakamoto, Intergranular li metal propagation through polycrystalline li6.25al0.25la3zr2o12 ceramic electrolyte, Electrochimica Acta 223 (2017) 85–91.

[33] J.-Y. Wu, V. P. Nguyen, C. T. Nguyen, D. Sutula, S. Sinaie, S. Bordas, Phase-field modeling of fracture, Adv. Appl. Math. Mech., Elsevier, 2019.

[34] A. Kumar, B. Bourdin, G. A. Francfort, O. Lopez-Pamies, Revisiting nucleation in the phase-field approach to brittle fracture, J. Mech. Phys. Solids 142 (2020) 104027.

[35] H. Amor, J.-J. Marigo, C. Maurini, Regularized formulation of the variational brittle fracture with unilateral contact: Numerical experiments, J. Mech. Phys. Solids 57 (8) (2009) 1209 – 1229.

[36] C. Miehe, M. Hofacker, F. Welschinger, A phase field model for rate-independent crack propagation: Robust algorithmic implementation based on operator splits, Comput. Methods Appl. Mech. Eng. 199 (45) (2010) 2765 – 2778.

[37] S. Rezaei, J. R. Mianroodi, T. Brepols, S. Reese, Direction-dependent fracture in solids: Atomistically calibrated phase-field and cohesive zone model, Journal of the Mechanics and Physics of Solids 147 (2021) 104253.

[38] Nguyen T. T., Yvonnet J., Bornert M., Chateau C., Sab K., Romani R., Le Roy R., On the choice of parameters in the phase field method for simulating crack initiation with experimental validation, International Journal of Fracture 197 (2) (2016) 213–226.

[39] E. Tanné, T. Li, B. Bourdin, J.-J. Marigo, C. Maurini, Crack nucleation in variational phase-field models of brittle fracture, J. Mech. Phys. Solids 110 (2018) 80 – 99.

[40] X. Zhang, C. Vignes, S. W. Sloan, D. Sheng, Numerical evaluation of the phase-field model for brittle fracture with emphasis on the length scale, Computational Mechanics (2017).

[41] T. Q. Bui, X. Hu, A review of phase-field models, fundamentals and their applications to composite laminates, Engineering Fracture Mechanics 248 (2021) 107705.

[42] E. Lorentz, S. Cuvilliez, K. Kazymyrenko, Convergence of a gradient damage model toward a cohesive zone model, Comptes Rendus Mécanique 339 (1) (2011) 20 – 26.

[43] S. May, J. Vignollet, R. de Borst, A numerical assessment of phase-field models for brittle and cohesive fracture: γ-convergence and stress oscillations, European Journal of Mechanics - A/Solids 52 (2015) 72–84.

[44] F. Freddi, F. Iurlano, Numerical insight of a variational smeared approach to cohesive fracture, J. Mech. Phys. Solids 98 (2017) 156 – 171.

[45] J.-Y. Wu, V. P. Nguyen, A length scale insensitive phase-field damage model for brittle fracture, J. Mech. Phys. Solids 119 (2018) 20 – 42.

[46] R. J. Geelen, Y. Liu, T. Hu, M. R. Tupek, J. E. Dolbow, A phase-field formulation for dynamic cohesive fracture, Comput. Methods Appl. Mech. Eng. 348 (2019) 680 – 711.

[47] S. Rezaei, A. Harandi, T. Brepols, S. Reese, An anisotropic cohesive fracture model: Advantages and limitations of length-scale insensitive phase-field damage models, Engineering Fracture Mechanics 261 (2022) 108177.

[48] C. Miehe, H. Dal, L.-M. Schänzel, A. Raina, A phase-field model for chemo-mechanical induced fracture in lithium-ion battery electrode particles, International Journal for Numerical Methods in Engineering 106 (2016) 683–711.

[49] X. Zhang, A. Krischok, C. R. Linder, A variational framework to model diffusion induced large plastic deformation and phase field fracture during initial two-phase lithiation of silicon electrodes, Computer Methods in Applied Mechanics and Engineering 312 (2016) 51–77.

[50] H. Yang, F. Fan, W. Liang, X. Guo, T. Zhu, S. Zhang, A chemo-mechanical model of lithiation in silicon, Journal of the Mechanics and Physics of Solids 70 (2014) 349 – 361.

[51] P. Zuo, Y. Zhao, A phase field model coupling lithium diffusion and stress evolution with crack propagation and application in lithium ion batteries., Physical chemistry chemical physics : PCCP 17 1 (2015).

[52] M. Klinsmann, D. Rosato, M. Kamlah, R. M. McMeeking, Modeling crack growth during li extraction and insertion within the second half cycle, Journal of Power Sources 331 (2016) 32–42.

[53] M. Klinsmann, D. Rosato, M. Kamlah, R. M. McMeeking, Modeling crack growth during li extraction in storage particles using a fracture phase field approach 163 (2) (2015) A102–A118.

[54] D. O'Connor, M. J. P. Welland, W. K. Liu, P. W. Voorhees, Phase transformation and fracture in single li x fepo 4 cathode particles: a phase-field approach to li–ion intercalation and fracture, Modelling and Simulation in Materials Science and Engineering 24 (2016) 035020.

[55] B.-X. Xu, Y. Zhao, P. Stein, Phase field modeling of electrochemically induced fracture in li-ion battery with large deformation and phase segregation, GAMM-Mitteilungen 39 (1) (2016) 92–109.

[56] A. Mesgarnejad, A. Karma, Phase field modeling of chemomechanical fracture of intercalation electrodes: Role of charging rate and dimensionality, Journal of the Mechanics and Physics of Solids 132 (2019) 103696.

[57] S. Narayan, L. Anand, On modeling the detrimental effects of inhomogeneous plating-and-stripping at a lithium-metal/solid-electrolyte interface in a solid-state-battery, Journal of The Electrochemical Society 167 (4) 040525.

[58] B. Liu, J. Xu, Cracks of silicon nanoparticles in anodes: Mechanics–electrochemical-coupled modeling framework based on the phase-field method, ACS Applied Energy Materials 3 (11) (2020) 10931–10939.

[59] A. M. Boyce, E. Martínez-Pañeda, A. Wade, Y. S. Zhang, J. J. Bailey, T. M. Heenan, D. J. Brett, P. R. Shearing, Cracking predictions of lithium-ion battery electrodes by x-ray computed tomography and modelling, Journal of Power Sources 526 (2022) 231119.

[60] A. F. Bower, P. R. Guduru, A simple finite element model of diffusion, finite deformation, plasticity and fracture in lithium ion insertion electrode materials, Modelling and Simulation in Materials Science and Engineering 20 (2012) 045004.

[61] G. Bucci, T. N. N. Swamy, Y.-M. Chiang, W. C. Carter, Modeling of internal mechanical failure of all-solid-state batteries during electrochemical cycling, and implications for battery design, Journal of Materials Chemistry 5 (2017) 19422–19430.

[62] N. Iqbal, Y. Ali, S. Lee, Debonding mechanisms at the particle-binder interface in the li-ion battery electrode 167 (6) (2020) 060515.

[63] Y. Bai, D. A. Santos, S. Rezaei, P. Stein, S. Banerjee, B.-X. Xu, A chemo-mechanical damage model at large deformation: numerical and experimental studies on polycrystalline energy materials, International Journal of Solids and Structures (2021) 111099.

[64] A. Singh, S. Pal, Chemo-mechanical modeling of inter- and intra-granular fracture in heterogeneous cathode with polycrystalline particles for lithium-ion battery, Journal of the Mechanics and Physics of Solids 163 (2022) 104839.

[65] T. Nguyen, J. Yvonnet, Q.-Z. Zhu, M. Bornert, C. Chateau, A phase-field method for computational modeling of interfacial damage interacting with crack propagation in realistic microstructures obtained by microtomography, Comput. Methods Appl. Mech. Eng. 312 (2016) 567 – 595.

[66] C. V. Di Leo, L. Anand, Hydrogen in metals: A coupled theory for species diffusion and large elastic–plastic deformations, Int. J. Plast 43 (2013) 42 – 69.

[67] A. Salvadori, R. McMeeking, D. Grazioli, M. Magri, A coupled model of transport-reaction-mechanics with trapping. part i – small strain analysis, J. Mech. Phys. Solids 114 (2018) 1 – 30.

[68] E. Martínez-Pañeda, A. Golahmar, C. F. Niordson, A phase field formulation for hydrogen assisted cracking, Comput. Methods Appl. Mech. Eng. 342 (2018) 742 – 761.

[69] F. Duda, A. Ciarbonetti, S. Toro, A. Huespe, A phase-field model for solute-assisted brittle fracture in elastic-plastic solids, International Journal of Plasticity 102 (2018) 16 – 40.

[70] L. Anand, Y. Mao, B. Talamini, On modeling fracture of ferritic steels due to hydrogen embrittlement, J. Mech. Phys. Solids 122 (2019) 280 – 314.

[71] H. Yu, J. S. Olsen, A. Alvaro, L. Qiao, J. He, Z. Zhang, Hydrogen informed gurson model for hydrogen embrittlement simulation, Engineering Fracture Mechanics 217 (2019) 106542.

[72] L. Sultanova, Łukasz Figiel, Microscale diffusion-mechanics model for a polymer-based solid-state battery cathode, Computational Materials Science 186 (2021) 109990.

[73] J.-Y. Wu, T. K. Mandal, V. P. Nguyen, A phase-field regularized cohesive zone model for hydrogen assisted cracking, Comput. Methods Appl. Mech. Eng. 358 (2020) 112614.

[74] R. Koerver, W. Zhang, L. de Biasi, S. Schweidler, A. O. Kondrakov, S. Kolling, T. Brezesinski, P. Hartmann, W. G. Zeier, J. Janek, Chemo-mechanical expansion of lithium electrode materials – on the route to mechanically optimized all-solid-state batteries, Energy Environ. Sci. 11 (2018) 2142–2158.

[75] T. K. Mandal, V. P. Nguyen, J.-Y. Wu, Comparative study of phase-field damage models for hydrogen assisted cracking, Theoretical and Applied Fracture Mechanics 111 (2021) 102840.

[76] Y. Zhao, P. Stein, B.-X. Xu, Isogeometric analysis of mechanically coupled cahn–hilliard phase segregation in hyperelastic electrodes of li-ion batteries, Computer Methods in Applied Mechanics and Engineering 297 (2015) 325 – 347.

[77] Y. Bai, Y. Zhao, W. Liu, B.-X. Xu, Two-level modeling of lithium-ion batteries, Journal of Power Sources 422 (2019) 92–103.

[78] Y. Luo, Y. Bai, A. Mistry, Y. Zhang, D. Zhao, S. Sarkar, J. V. Handy, S. Rezaei, A. C. Chuang, L. Carrillo, K. Wiaderek, M. Pharr, K. Xie, P. P. Mukherjee, B.-X. Xu, S. Banerjee, Effect of crystallite geometries on electrochemical performance of porous intercalation electrodes by multiscale operando investigation, Nature Materials (2022).

[79] C. Kuhn, A. Schlüter, R. Müller, On degradation functions in phase field fracture models, Computational Materials Science 108 (2015) 374–384, selected Articles from Phase-field Method 2014 International Seminar.

[80] L. Svolos, C. A. Bronkhorst, H. Waisman, Thermal-conductivity degradation across cracks in coupled thermo-mechanical systems modeled by the phase-field fracture method, Journal of the Mechanics and Physics of Solids 137 (2020) 103861.

[81] P. Stein, Y. Zhao, B.-X. Xu, Effects of surface tension and electrochemical reactions in li-ion battery electrode nanoparticles, Journal of Power Sources 332 (2016) 154–169.

[82] X. Song, Y. Lu, F. Wang, X. Zhao, H. Chen, A coupled electro-chemo-mechanical model for all-solid-state thin film li-ion batteries: The effects of bending on battery performances, Journal of Power Sources 452 (2020) 227803.

[83] T. H. Wan, F. Ciucci, Electro-chemo-mechanical modeling of solid-state batteries, Electrochimica Acta 331 (2020) 135355.

[84] H. Fathiannasab, L. Zhu, Z. Chen, Chemo-mechanical modeling of stress evolution in all-solid-state lithium-ion batteries using synchrotron transmission x-ray microscopy tomography, Journal of Power Sources 483 (2021) 229028.

[85] D. Gaston, C. Newman, G. Hansen, D. Lebrun-Grandie, Moose: A parallel computational framework for coupled systems of nonlinear equations, Nuclear Engineering and Design 239 (10) (2009) 1768–1778.

[86] C. J. Permann, D. R. Gaston, D. Andrš, R. W. Carlsen, F. Kong, A. D. Lindsay, J. M. Miller, J. W. Peterson, A. E. Slaughter, R. H. Stogner, R. C. Martineau, MOOSE: Enabling massively parallel multiphysics simulation, SoftwareX 11 (2020) 100430.

[87] S. Balay, S. Abhyankar, M. F. Adams, J. Brown, P. Brune, K. Buschelman, L. Dalcin, A. Dener, V. Eijkhout, W. D. Gropp, D. Karpeyev, D. Kaushik, M. G. Knepley, D. A. May, L. C. McInnes, R. T. Mills, T. Munson, K. Rupp, P. Sanan, B. F. Smith, S. Zampini, H. Zhang, H. Zhang, PETSc users manual, Tech. rep., Argonne National Laboratory (2019).

[88] T. Hu, J. Guilleminot, J. E. Dolbow, A phase-field model of fracture with frictionless contact and random fracture properties: Application to thin-film fracture and soil desiccation, Computer Methods in Applied Mechanics and Engineering 368 (2020) 113106.

[89] `https://github.com/hugary1995/raccoon`, GitHub.

[90] C. Geuzaine, J.-F. Remacle, Gmsh: A 3-d finite element mesh generator with built-in pre- and post-processing facilities, International Journal for Numerical Methods in Engineering 79 (2009) 1309 – 1331.

[91] J. P. Ahrens, B. Geveci, C. C. Law, Paraview: An end-user tool for large-data visualization, in: The Visualization Handbook, 2005.

[92] A. Lindsay, R. Stogner, D. Gaston, D. Schwen, C. Matthews, W. Jiang, L. K. Aagesen, R. Carlsen, F. Kong, A. Slaughter, C. Permann, R. Martineau, Automatic differentiation in metaphysicl and its applications in moose, Nuclear Technology 207 (7) (2021) 905–922.

[93] D. R. Gaston, C. J. Permann, J. W. Peterson, A. E. Slaughter, D. Andrš, Y. Wang, M. P. Short, D. M. Perez, M. R. Tonks, J. Ortensi, L. Zou, R. C. Martineau, Physics-based multiscale coupling for full core nuclear reactor simulation, Annals of Nuclear Energy 84 (2015) 45–54.

[94] Y. Luo, S. Rezaei, D. A. Santos, Y. Zhang, J. V. Handy, L. Carrillo, B. J. Schultz, L. Gobbato, M. Pupucevski, K. Wiaderek, H. Charalambous, A. Yakovenko, M. Pharr, B.-X. Xu, S. Banerjee, Cation reordering instead of phase transitions: Origins and implications of contrasting lithiation mechanisms in 1d ζ- and 2d α-v¡sub¿2¡/sub¿o¡sub¿5¡/sub¿, Proceedings of the National Academy of Sciences 119 (4) (2022) e2115072119.

[95] P. Shanthraj, B. Svendsen, L. Sharma, F. Roters, D. Raabe, Elasto-viscoplastic phase field modelling of anisotropic cleavage fracture, Journal of the Mechanics and Physics of Solids 99 (2017) 19–34.

[96] D. Carlstedt, K. Runesson, F. Larsson, L. E. Asp, On the coupled thermo–electro–chemo–mechanical performance of structural batteries with emphasis on thermal effects, European Journal of Mechanics - A/Solids 94 (2022) 104586.

[97] K. Khaledi, S. Rezaei, S. Wulfinghoff, S. Reese, A microscale finite element model for joining of metals by large plastic deformations, Comptes Rendus Mécanique 346 (8) (2018) 743–755.

[98] H. Ruan, S. Rezaei, Y. Yang, D. Gross, B.-X. Xu, A thermo-mechanical phase-field fracture model: Application to hot cracking simulations in additive manufacturing, Journal of the Mechanics and Physics of Solids (2022) 105169.

[99] M. G. Boebinger, D. Yeh, M. Xu, B. C. Miles, B. Wang, M. Papakyriakou, J. A. Lewis, N. P. Kondekar, F. J. Q. Cortes, S. Hwang, X. Sang, D. Su, R. R. Unocic, S. Xia, T. Zhu, M. T. McDowell, Avoiding fracture in a conversion battery material through reaction with larger ions, Joule 2 (9) (2018) 1783–1799.

[100] L. Schöller, D. Schneider, C. Herrmann, A. Prahs, B. Nestler, Phase-field modeling of crack propagation in heterogeneous materials with multiple crack order parameters, Computer Methods in Applied Mechanics and Engineering 395 (2022) 114965.

[101] J. E. Ni, E. D. Case, J. S. Sakamoto, E. Rangasamy, J. B. Wolfenstine, Room temperature elastic moduli and vickers hardness of hot-pressed llzo cubic garnet, Journal of Materials Science 47 (23) (2012) 7978–7985.

[102] S. Rezaei, D. Jaworek, J. R. Mianroodi, S. Wulfinghoff, S. Reese, Atomistically motivated interface model to account for coupled plasticity and damage at grain boundaries, Journal of the Mechanics and Physics of Solids 124 (2019) 325 – 349.

[103] S. Daubner, M. Weichel, D. Schneider, B. Nestler, Modeling intercalation in cathode materials with phase-field methods: Assumptions and implications using the example of lifepo4, Electrochimica Acta (2022) 140516.

[104] S. Monismith, J. Qu, R. Dingreville, Grain-boundary fracture mechanisms in li7la3zr2o12 (llzo) solid electrolytes: When phase transformation acts as a temperature-dependent toughening mechanism, Journal of the Mechanics and Physics of Solids 160 (2022) 104791.

[105] L. Cabras, D. Danilov, W. Subber, V. Oancea, A. Salvadori, A two-mechanism and multiscale compatible approach for solid state electrolytes of (li-ion) batteries, Journal of Energy Storage 48 (2022) 103842.